

Dynamical Controls on Bottom Water Transport and Transformation across the Antarctic Circumpolar Current

CARLYN R. SCHMIDGALL,^a YIDONGFANG SI,^a ANDREW L. STEWART,^a ANDREW F. THOMPSON,^b
AND ANDREW MCC. HOGG^c

^a *Department of Atmospheric and Oceanic Sciences, University of California, Los Angeles, Los Angeles, California*

^b *Environmental Sciences and Engineering, California Institute of Technology, Pasadena, California*

^c *Research School of Earth Sciences and Australian Research Council Centre of Excellence for Climate Extremes, Australian National University, Canberra, Australian Capital Territory, Australia*

(Manuscript received 27 May 2022, in final form 31 March 2023, accepted 25 April 2023)

ABSTRACT: The export of Antarctic Bottom Water (AABW) supplies the bottom cell of the global overturning circulation and plays a key role in regulating climate. This AABW outflow must cross, and is therefore mediated by, the Antarctic Circumpolar Current (ACC). Previous studies present widely varying conceptions of the role of the ACC in directing AABW across the Southern Ocean, suggesting either that AABW may be zonally recirculated by the ACC, or that AABW may flow northward within deep western boundary currents (DWBC) against bathymetry. In this study the authors investigate how the forcing and geometry of the ACC influences the transport and transformation of AABW using a suite of process-oriented model simulations. The model exhibits a strong dependence on the elevation of bathymetry relative to AABW layer thickness: higher meridional ridges suppress zonal AABW exchange, increase the strength of flow in the DWBC, and reduce the meridional variation in AABW density across the ACC. Furthermore, the transport and transformation vary with density within the AABW layer, with denser varieties of AABW being less efficiently transported between basins. These findings indicate that changes in the thickness of the AABW layer, for example, due to changes in Antarctic shelf processes, and tectonic changes in the sea floor shape may alter the pathways and transformation of AABW across the ACC.

SIGNIFICANCE STATEMENT: The ocean plays an outsized role in the movement of heat and trace gases around Earth, and the northward export of dense Antarctic Bottom Water is a crucial component of this climate-regulating process. This study aims to understand what sets the pathways of Antarctic Bottom Water as it travels northward across the Antarctic Circumpolar Current, and thus what controls its partitioning between the Atlantic, Indian, and Pacific basins. Our results highlight the importance of seafloor elevation relative to the thickness of the Antarctic Bottom Water layer for directing the flow northward versus between basins. This study motivates future investigation of long-term changes in Antarctic Bottom Water properties and their consequences for its global distribution.

KEYWORDS: Southern Ocean; Abyssal circulation; Idealized models

1. Introduction

The global circulation of Antarctic Bottom Water (AABW) is often quantified via transport streamfunction in a two-dimensional, latitude/depth space (e.g., Lumpkin and Speer 2007). However, its formation, northward flow, and distribution between the Atlantic, Indian, and Pacific basins are fundamentally three-dimensional processes. AABW is formed in a handful of distinct sites around the Antarctic coast, notably the southern Weddell Sea (Nicholls et al. 2009), the western Ross Sea (Gordon et al. 2004), along the Adélie coast (Rintoul 1985; Williams et al. 2010), and in Prydz Bay (Ohshima et al. 2013). The net export of AABW is also asymmetrically distributed between the major ocean basins (Johnson 2008): ~ 4 Sv ($1 \text{ Sv} \equiv 10^6 \text{ m}^3 \text{ s}^{-1}$) flows northward into the Atlantic Ocean, in contrast with ~ 12 and ~ 14 Sv entering the Indian and Pacific Oceans, respectively (Talley 2013). A consequence of this asymmetry is that the AABW-driven cell of the global overturning circulation is concentrated in the Indo-Pacific,

with the Atlantic being dominated by the North Atlantic Deep Water-driven cell (Lumpkin and Speer 2007; Talley 2013). Figure 1 illustrates the complexity of these three-dimensional connections via climatological maps of the depth of the 28.2 kg m^{-3} neutral density surface, an approximate upper bound for the AABW layer, and of the seafloor oxygen concentration in the Southern Ocean.

The connectivity between Antarctic shelf sources of AABW and the major ocean basins dictates the response of the global overturning circulation to localized changes in AABW formation. Such changes might arise, for example, in response to major glacier calving events (Snow et al. 2018), due to variability in the density and export rates of dense shelf waters (Purkey and Johnson 2013; Abrahamsen et al. 2019), due to anthropogenically driven shutdown of one or more of the current dense water formation sites (Hellmer et al. 2012, 2017), or due to variability in the formation of deep waters via open-ocean convection (de Lavergne et al. 2014). Significant shifts in the three-dimensional structure of the global overturning circulation have also been associated with major climate shifts, such as the transition between glacial and interglacial periods (Ferrari et al. 2014; Thompson et al. 2016).

Corresponding author: Carlyn R. Schmidgall, crschmid@uw.edu

DOI: 10.1175/JPO-D-22-0113.1

© 2023 American Meteorological Society. This published article is licensed under the terms of the default AMS reuse license. For information regarding reuse of this content and general copyright information, consult the AMS Copyright Policy (www.ametsoc.org/PUBSReuseLicenses).

Brought to you by MIT LIBRARIES | Unauthenticated | Downloaded 02/06/25 07:04 PM UTC

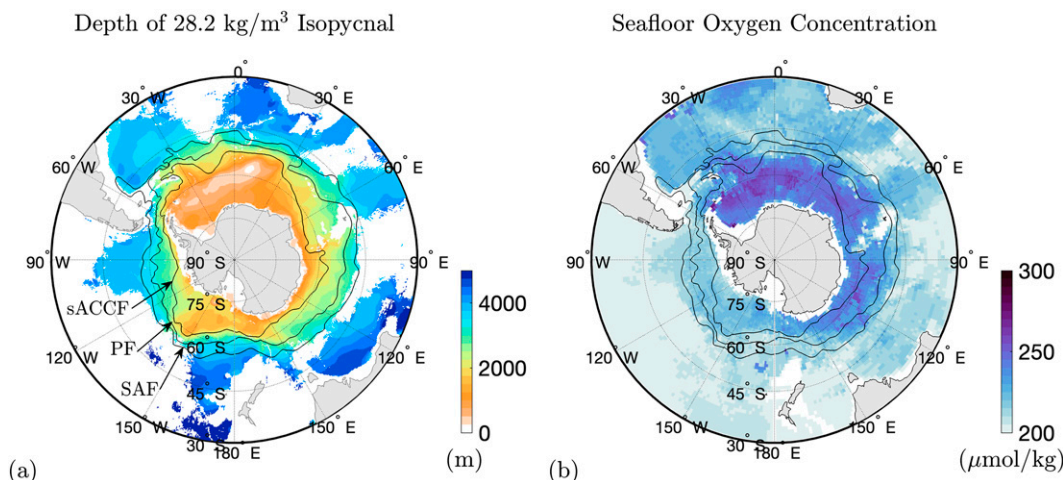


FIG. 1. Observations of quantities indicating AABW spread across the Southern Ocean and into the abyssal ocean basins: (a) statistical mean depth of the 28.2 kg m^{-3} neutral density surface on a $1/4^\circ$ grid, and (b) statistical mean seafloor dissolved oxygen concentrations in the Southern Ocean on a 1° grid. Data are taken from *World Ocean Atlas 2018* (Garcia et al. 2018; Locarnini et al. 2019) with neutral density computed following Jackett and McDougall (1997). Solid black contours indicate Southern Ocean frontal locations: from south to north, the southern ACC Front (sACCF), Polar Front (PF), and Subantarctic Front (SAF) from Orsi et al. (1995).

All northward flow of AABW that reaches the northern basins must cross the Antarctic Circumpolar Current (ACC). This suggests that the ACC plays a key role in mediating connections between AABW shelf sources and the northern basins. Previous model-based studies have attempted to quantify the pathways of AABW across the ACC but have produced conflicting results. For example, van Sebille et al. (2013) deployed Lagrangian particles at the ocean surface around Antarctica and tracked those that flowed northward in the AABW layer. They found that water parcels in the AABW layer underwent at least one full circuit around the Antarctic continent as they traversed the ACC, and therefore that the ACC served to “blend” all AABW sources together before they reached the northern basins. In contrast, Kushara et al. (2017) deployed nine different passive tracer concentrations in dense water formation sites in a regional ocean–sea ice model. By tracking these tracers, they inferred that shelf-sourced AABW crosses the ACC in a series of deep western boundary currents, or “conduits,” supported by major bathymetric features. Recent modeling work by Solodoch et al. (2022) demonstrates the importance of these conduits in determining the fate of AABW sourced from different locations around the Antarctic continental margins. By deploying tracers at four major AABW formation sites in a global ocean/sea ice model, they found that AABW formed in the Weddell Sea and Prydz Bay is blended together before export mainly to the Atlantic and Indian Oceans, whereas AABW originating in the Ross Sea and Adelie Land is exported primarily to the Pacific Ocean. Measurements of AABW in the ACC are too sparse to distinguish between these conduit and blender paradigms. For example, observational tracer-based methods can effectively track the global spread of AABW as a whole but have not yet been able to distinguish between waters sourced from different sectors of the Antarctic

continental shelf (Orsi et al. 1999; Johnson 2008; Cimoli et al. 2023).

Figure 2 illustrates two extreme conceptual descriptions of the ACC’s role in mediating northward transport of AABW, based on these previous studies. Around major bathymetric features, sketched here as a simple meridional ridge, the ACC is deflected north following contours of planetary potential vorticity (f/H), and forms a meander that is offset slightly to the east of the ridge (Hallberg and Gnanadesikan 2001; Viebahn and Eden 2012; Thompson and Naveira Garabato 2014). Figure 2a illustrates the conduit conception (e.g., Kushara et al. 2017), in which the AABW outflow forms a deep western boundary current, with no zonal exchange across the ridge. In this configuration bathymetric features separate different varieties of AABW, directing them toward different ocean basins. Figure 2b shows another extreme, in which AABW is transported over the ridge and blended between different sectors of the ACC as it travels northward (e.g., van Sebille et al. 2013). In this configuration the northward flow may be expected to be less localized: for example, in the limit of a completely flat sea floor the transport would be evenly distributed in longitude and carried by mesoscale eddies (Abernathey et al. 2011; Stewart and Thompson 2013). In this study we will show that the height of topographic obstacles plays an important role in shifting the ACC between the two regimes sketched in Fig. 2.

This study aims to elucidate the dynamics of AABW pathways across the Southern Ocean and identify key controls on its meridional versus interbasin transports. Previous theoretical studies on this topic have typically adopted a zonally averaged description of the dynamics (e.g., Ito and Marshall 2008; Nikurashin and Vallis 2011, 2012; Stewart et al. 2014; Thompson et al. 2016; Chang and Jansen 2021), and thus have not specifically considered meridional versus interbasin transports of AABW. However, these studies provide important insights that

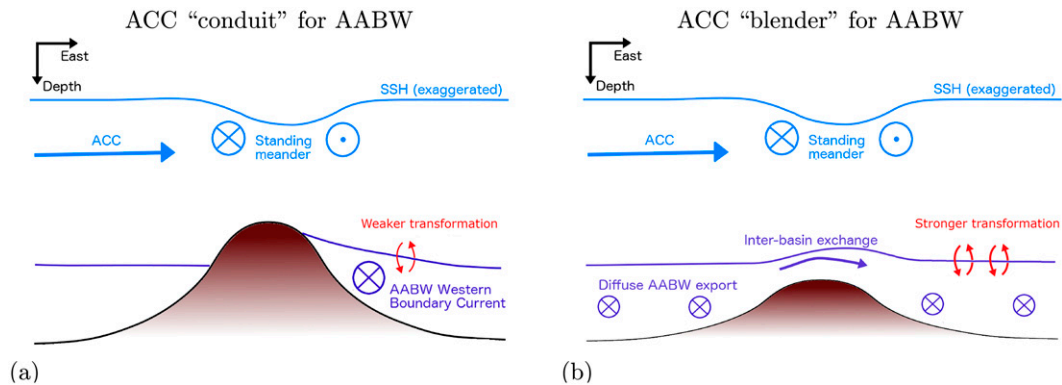


FIG. 2. Schematic of the conduit and blender conceptualizations of the ACC's role in mediating AABW export. Where the ACC encounters major bathymetric features, it forms a standing meander, characterized by anomalously low sea surface height (SSH) and cyclonic flow (dot indicates flow out of the page, and cross indicates flow into the page) around the bathymetry. (a) For a relatively thin AABW layer or high bathymetric ridge, AABW crosses the ACC northward as a steady deep western boundary current, and this more direct path results in less cumulative transformation of AABW. (b) A relatively thick AABW layer or low bathymetric ridge allows the ACC to drive an efficient zonal transfer of AABW between ocean basins, corresponding to enhanced cumulative transformation of AABW layer as it is zonally recirculated.

guide our approach. For example, due to the incropping of isopycnals at the sea floor, the northward transport of AABW is intrinsically linked to the rate of diapycnal upwelling (Ito and Marshall 2008; Broadbridge et al. 2016). In the following sections we therefore give due attention to both the transport and transformation of AABW in the ACC, and their relationship with one another.

Building on these previous findings, in this study we investigate dynamical controls on meridional versus interbasin transport of AABW using a suite of eddy-resolving process-oriented simulations of an idealized sector of the Southern Ocean. In section 2 we describe the model configuration, rationalize the suite of experiments, and discuss diagnostics of the meridional and interbasin transports of AABW. In section 3 we quantify the sensitivity of meridional and interbasin transports, integrated across the entire AABW layer, and identify key controls on the ratio of these transports. In section 4 we examine the density dependence of the meridional versus interbasin transports within the AABW layer, and link these to the rates of transformation of AABW. In section 5 we summarize our key findings and discuss their implications.

2. Methods

a. Model configuration and experiments

Our aim is to construct an idealized model that captures the key features of AABW circulation in the Southern Ocean. This approach provides a clear view of the physics, unobstructed by the complexities of the full geometry and water-mass structure that are present in nature. The model domain, illustrated in Fig. 3a, is a 4000-km-long, 2500-km-wide, 4000-m-deep reentrant channel with a 500-m-deep Antarctic continental shelf along its southern margin, separated by a 150-km-wide continental slope that is centered at $y = 300$ km. This setup extends configurations used by Stewart and Thompson (2012, 2013) and Stewart and

Hogg (2017) by including a 200-km-wide continental barrier, extending from the northern boundary down to $y = 1500$ km. The “continent” is connected to the continental slope via a 3000-m-deep, ~ 400 -km-wide meridional ridge. In some experiments we superpose additional Gaussian topographic bumps throughout the model domain, with a typical wavelength of 200 km. The pattern of bumps is set randomly for each experiment. The resulting geometry is similar to those used by Morrison and Hogg (2013) and Wilson et al. (2022) and allows quantification of zonal exchange between “basins” (i.e., across the ridge) while avoiding direct interaction between the zonal throughflow and the northern boundary. The model domain may be thought of as an idealization of the region around Drake Passage or around other bathymetric obstacles in the path of the ACC, such as Kerguelen Plateau or Macquarie Ridge.

We simulate the state and circulation of the ocean by solving the Boussinesq primitive equations (e.g., Vallis 2006) using the MIT general circulation model (MITgcm; Marshall et al. 1997b,a). We simplify the thermodynamics by eliminating the dependence of density on salinity, and relating density to potential temperature via a linear equation of state with a thermal expansion coefficient of $\alpha = 1.5 \times 10^{-4} \text{ } ^\circ\text{C}^{-1}$. The model is forced by idealized, time-invariant latitudinal profiles of surface buoyancy flux (Fig. 3b) and zonal wind stress (Fig. 3c), motivated by observed conditions in the Southern Ocean (Large and Yeager 2009). Specifically, we impose a downward surface heat flux south of $y = 1500$ km, with a maximum of 10 W m^{-2} at $y = 800$ km, and an upward surface heat flux north of $y = 1500$ km, with a maximum of 10 W m^{-2} at $y = 1950$ km. The wind stress is eastward over most of the model domain ($y > 500$ km), with a maximum of 0.15 N m^{-2} at $y = 1600$ km, and is directed westward over the Antarctic continental shelf and slope ($y < 500$ km), with a maximum amplitude of 0.075 N m^{-2} at $y = 225$ km.

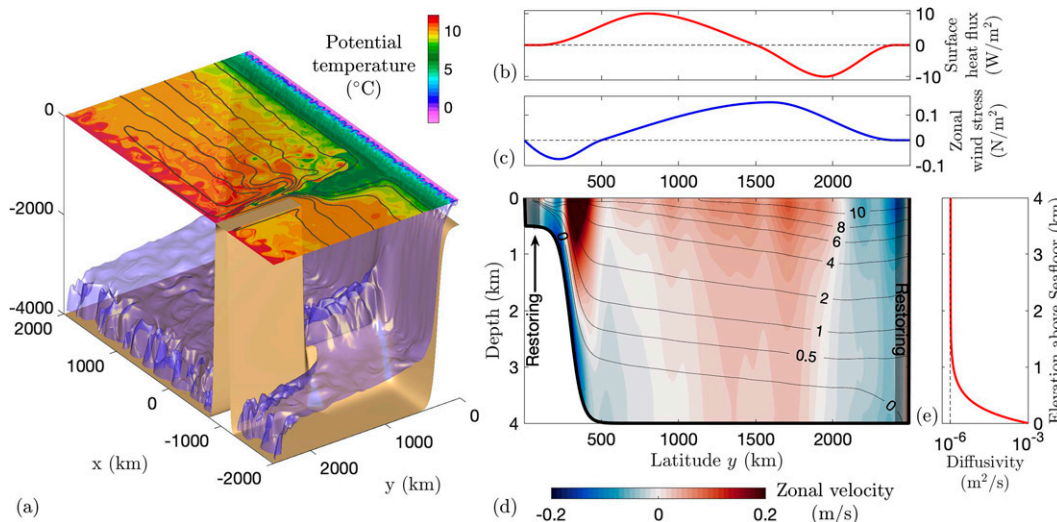


FIG. 3. Configuration of a process-oriented model of AABW export across the ACC: (a) three-dimensional rendering of the model domain, showing the bathymetry (light-brown surface), a snapshot of the top of the AABW layer ($\theta = 0^\circ\text{C}$; translucent blue), a concurrent snapshot of sea surface temperature (colors), and time-mean sea surface height contours (dark-gray lines); profiles of (b) downward surface heat flux and (c) eastward wind stress applied at the sea surface; (d) time- and zonal-mean zonal velocity (colors) and potential temperature ($^\circ\text{C}$; contours), with regions of stratification restoring highlighted at the meridional boundaries; and (e) profile of vertical diffusivity with elevation above sea floor.

On the Antarctic continental shelf, dense water is formed via restoring toward a potential temperature of -1°C within 100 km of the southern boundary (see Fig. 3d). Within 100 km of the northern boundary, we restore the potential temperature toward a profile that varies exponentially from 12°C at the surface to 0°C at the sea floor, with an e -folding scale of 1000 m. The northern boundary is closed, such that meridional velocity is gradually set to zero across the 100-km sponge layer. To allow transformation of AABW as it crosses the ACC, we impose a spatially varying vertical diffusivity κ that decreases upward from the sea floor with an exponential decay scale of 300 m, and a maximum value of $10^{-3} \text{ m}^2 \text{ s}^{-1}$ (Mashayek et al. 2017). Additionally, we set a minimum background vertical diffusivity of $5 \times 10^{-6} \text{ m}^2 \text{ s}^{-1}$ throughout the model domain. The bottom-enhanced diffusivity profile and the background diffusivity are shown in Fig. 3e. Near-surface turbulent mixing and shear-driven mixing in the subsurface are prescribed via the K-profile parameterization (Large et al. 1994). We use a second-order-moment Prather scheme to advect potential temperature, which minimizes spurious diapycnal mixing (Prather 1986; Hill et al. 2012).

The model equations are discretized into 70 vertical levels with spacings ranging from ~ 10 m at the surface to ~ 100 m at 4000-m depth. Simulations run with a coarser horizontal spacings of ~ 10 km were integrated until the simulations reached a statistically steady state, which was determined using domain-averaged annual snapshots of potential temperature and typically achieved within 60–100 model years. These coarse-resolution simulations were used to spin-up the corresponding higher-resolution runs with ~ 5 -km horizontal spacings, typically requiring an additional 40 years of integration. The high-

resolution runs can be considered eddy resolving, as the Rossby radius varies from ~ 16 to 21 km north of the continental slope. All diagnostics discussed below are computed from the higher-resolution runs, using a 20-yr time-average of integration in statistically steady state.

Figures 3a and 3d illustrate the simulated state and circulation in the reference simulation, defined by the model parameters listed in Table 1. The stratification and zonal transport are qualitatively consistent with the ACC in nature: the isopycnals shoal to the south across the model domain, producing a surface-intensified eastward flow (Fig. 3d). The associated time-mean sea surface height contours, corresponding to streamlines of the surface geostrophic flow, form a pronounced meander in the lee of the ridge that qualitatively resembles those found in the ACC (Orsi et al. 1995; Thompson and Naveira Garabato 2014). Over the model's Antarctic continental slope, the imposed wind stress drives a westward Antarctic Slope Current (Thompson et al. 2018). The buoyancy gradient associated with dense water formation on the continental shelf produces a deep westward flow over the continental slope, associated with the downslope flow of dense water, and a relatively strong, near-surface eastward flow just north of the slope. The meridional overturning circulation is quantified and discussed in section 2b.

For the reference case, the model simulates an ACC transport of 120.3 Sv. This is comparable to observational estimates, which range between 173.3 Sv (Donohue et al. 2016) and 134 Sv (Whitworth and Peterson 1985). We partition the ACC transport into its barotropic component by diagnosing the bottom zonal velocity at each latitude and longitude, integrating with depth and latitude, and then averaging across the longitude band of Drake Passage, $-1100 \leq x \leq -900$ km.

TABLE 1. List of key model configuration parameters used in the reference simulation. Parameters that are varied between experiments are indicated by an italicized description.

Parameter	Value	Description
L_x	4000 km	Zonal domain size
L_y	2500 km	Meridional domain size
H	4000 m	Max ocean depth
X_{ridge}	−1000 km	Zonal position of ridge/northern continent
W_{ridge}	400 km	Zonal width of ridge
H_{ridge}	1000 m	<i>Ridge height</i>
Y_{cont}	1500 km	Southernmost limit of northern continent
W_{cont}	200 km	Zonal width of northern continent
W_{NCS}	100 km	Width of northern continental slope
W_{ACS}	75 km	Antarctic continental slope half-width
Y_{ACS}	300 km	Lat of Antarctic continental slope
H_{shelf}	500 m	Continental shelf depth
L_{shelf}	100 km	Width of Antarctic continental shelf
L_{rand}	200 km	Random topography horizontal length scale
H_{rand}	0 m	<i>Random topography root-mean-square height</i>
L_{sponge}	100 km	Width of sponge layers
T_{sponge}	7 days	Sponge restoring time scale
θ_{shelf}	−1 °C	<i>Temperature of AABW on continental shelf</i>
τ_{ACC}	0.15 N m ^{−2}	<i>Max wind stress over ACC</i>
τ_{slope}	0.075 N m ^{−2}	Max wind stress over continental slope
Y_{wind}	1600 km	Lat of ACC wind stress max
f_0	$-1.32 \times 10^{-4} \text{ s}^{-1}$	Reference Coriolis parameter
β	$9.63 \times 10^{-12} \text{ m}^{-1} \text{ s}^{-1}$	Meridional gradient of Coriolis parameter
α	$1.5 \times 10^{-4} \text{ }^{\circ}\text{C}^{-1}$	Thermal expansion coef
r_b	$1.1 \times 10^{-3} \text{ m s}^{-1}$	Linear bottom drag coef
A_h	12 m ² s ^{−1}	Horizontal eddy viscosity
A_v	$3 \times 10^{-4} \text{ m}^2 \text{ s}^{-1}$	Vertical eddy viscosity
$A_{4\text{grid}}$	0.1	Grid-dependent biharmonic viscosity
κ_b	$5 \times 10^{-6} \text{ m}^2 \text{ s}^{-1}$	Background vertical diffusivity
κ_{max}	$1 \times 10^{-3} \text{ m}^2 \text{ s}^{-1}$	<i>Sea floor vertical diffusivity</i>
Δ_x, Δ_y	5.2 km	Horizontal grid spacing
Δ_z	10.5–103.8 m	Vertical grid spacing
Δ_t	313 s	Time step

The baroclinic component is taken as the difference between total ACC transport and the barotropic component. For the reference case, the model yields barotropic and baroclinic transports of 16.2 and 104.1 Sv, respectively. For cases with meridional ridges ≤ 500 m, the barotropic transport contributes a greater proportion of the total transport. Donohue et al. (2016) found that barotropic transport accounts for roughly 26% of the total transport through Drake Passage, a similar partitioning to that of the model configured with the 500-m ridge.

To investigate key controls on the transport and transformation of AABW, we perform a total of 24 model sensitivity experiments, listed in Table 2. We selected 5 key sensitivity parameters, identified via italics in Table 1, based on previous studies: we vary the meridional ridge height (H_{ridge}) because it serves as a physical barrier to zonal transport of AABW, and may be anticipated to support deep meridional boundary currents (Fukamachi et al. 2010; Kusahara et al. 2017; Stewart and Hogg 2017). We vary the sea floor diffusivity (κ_{max}) because bottom-enhanced mixing has been shown to play a key role in transformation of AABW (Mashayek et al. 2015; Yang et al. 2018). We vary the amplitude of the random bathymetric bumps (H_{rand}) (cf. Zhang and Nikurashin 2020; Jouanno

and Capet 2020), which have shown to produce higher effective diapycnal diffusivities far above the mean sea floor depth (Mashayek et al. 2017), and thus may be expected to contribute both to supporting geostrophic transport and to enhanced transformation of AABW. We vary the surface wind stress (τ_{max}) because, although we anticipate little sensitivity of the zonal transport to winds (Munday et al. 2013; Marshall et al. 2017), changes in mesoscale eddy activity in the lee of standing meanders may influence transport of AABW (Meredith and Hogg 2006; Fukamachi et al. 2010; Thompson and Naveira Garabato 2014). Last, we vary the potential temperature of AABW on the continental shelf (θ_{shelf}) as a proxy for changes in buoyancy loss, which in turn may be expected to influence the strength of the overturning circulation and strength of the zonal baroclinic transport of the ACC (Morrison et al. 2011, 2015; Howard et al. 2015; Behrens et al. 2016; Lynch-Stieglitz et al. 2016).

b. Quantifying meridional versus zonal transports of AABW

To visualize and quantify the transport of AABW in depth/latitude space, we compute a series of overturning streamfunctions, each capturing a component of the circulation (see

TABLE 2. List of model parameter combinations used in the experiments, as well as the dynamically defined AABW potential temperature boundary used in our analysis. The reference case is listed first. Boldface values indicate perturbations from reference parameters.

Ridge height H_{ridge} (m)	Random topographic amplitude H_{rand} (m)	Max wind stress τ (N m ⁻²)	Max sea floor diffusivity κ_{max} (m ² s ⁻¹)	Shelf AABW temperature θ_{shelf} (°C)	AABW temperature bound θ_{max} (°C)
1000	0	0.15	0.001	-1	0
0	0	0.15	0.001	-1	0
250	0	0.15	0.001	-1	0
500	0	0.15	0.001	-1	0
750	0	0.15	0.001	-1	0
1250	0	0.15	0.001	-1	0
1500	0	0.15	0.001	-1	0
2000	0	0.15	0.001	-1	0
1000	50	0.15	0.001	-1	0.05
1000	100	0.15	0.001	-1	0.1
1000	0	0.1	0.001	-1	0
1000	0	0.2	0.001	-1	0
1000	0	0.15	0.0001	-1	0
1000	0	0.15	0.0003	-1	0
1000	0	0.15	0.003	-1	0.15
1000	0	0.15	0.01	-1	0.5
1000	0	0.15	0.001	-0.75	0
1000	0	0.15	0.001	-0.5	0.1
0	50	0.15	0.001	-1	0.05
0	100	0.15	0.001	-1	0.2
500	50	0.15	0.001	-1	0.05
500	100	0.15	0.001	-1	0.15
500	0	0.1	0.001	-1	0
500	0	0.2	0.001	-1	0

Fig. 4). For each experiment, the isopycnal overturning streamfunction Ψ is computed by integrating meridional transports within temperature layers (Döös and Webb 1994; Wolfe 2014),

$$\Psi(y, \theta) = \overline{\int_{z=\eta_b}^{z=0} v \mathcal{H}[\tilde{\theta}(x, y, z, t) - \theta] dz}^{x, t}. \quad (1)$$

Here $\overline{\bullet}^{x, t}$ denotes a time average and zonal integral, \mathcal{H} denotes the Heaviside step function, and $z = \eta_b(x, y)$ denotes the sea floor. To clarify the notation, we distinguish the potential temperature coordinate θ from the spatially and temporally varying potential temperature field $\tilde{\theta}$ simulated by the model. In Figs. 4a and 4b we plot both $\Psi(y, \theta)$ and its counterpart in latitude/depth space, $\tilde{\Psi}(y, z)$, which we relate via a remapping of each potential temperature level to the time-/zonal-mean depth of the corresponding isotherm (Nurser and Lee 2004; Sun et al. 2020).

To identify the contributions of wind-driven Ekman transport, standing waves and transient eddies to the simulated overturning, we decompose the isopycnal overturning streamfunction. The mean component Ψ^m is computed by integrating time-averaged meridional transports within time-averaged potential temperature layers (see, e.g., Stewart and Thompson 2013; Wolfe 2014),

$$\Psi^m(y, \theta) = \overline{\int_{z=\eta_b}^{z=0} \bar{v}^t \mathcal{H}[\bar{\theta}^t(x, y, z) - \theta] dz}. \quad (2)$$

We then calculate the eddy component Ψ^e via the difference between the isopycnal and mean overturning streamfunctions,

$$\Psi^e(y, \theta) = \Psi(y, \theta) - \Psi^m(y, \theta). \quad (3)$$

We further decompose the mean component by computing the Eulerian mean circulation Ψ_{EM}^m , calculated by integrating zonally averaged velocity across the domain,

$$\tilde{\Psi}_{\text{EM}}^m(y, z) = \int_{z'=z}^{z'=0} \bar{v}^{x, t} dz', \quad (4)$$

where z' denotes a variable of integration. Note that we compute $\tilde{\Psi}_{\text{EM}}^m$ in latitude/depth space and then remap to potential temperature space to obtain Ψ_{EM}^m . We then define the “standing wave” streamfunction Ψ_{SW}^m as the difference between the total mean and Eulerian mean components,

$$\Psi_{\text{SW}}^m(y, \theta) = \Psi^m(y, \theta) - \Psi_{\text{EM}}^m(y, \theta). \quad (5)$$

This component of the streamfunction quantifies the isopycnal transport associated with deviations of the time-mean flow from the zonal/time-mean flow, which is also referred to as the “standing eddy” component of the flow or the “standing meanders” (Bischoff and Thompson 2014; Thompson and Naveira Garabato 2014).

Figure 4 shows features of the overturning circulation for the reference-case simulation. From Fig. 4a, we can see the

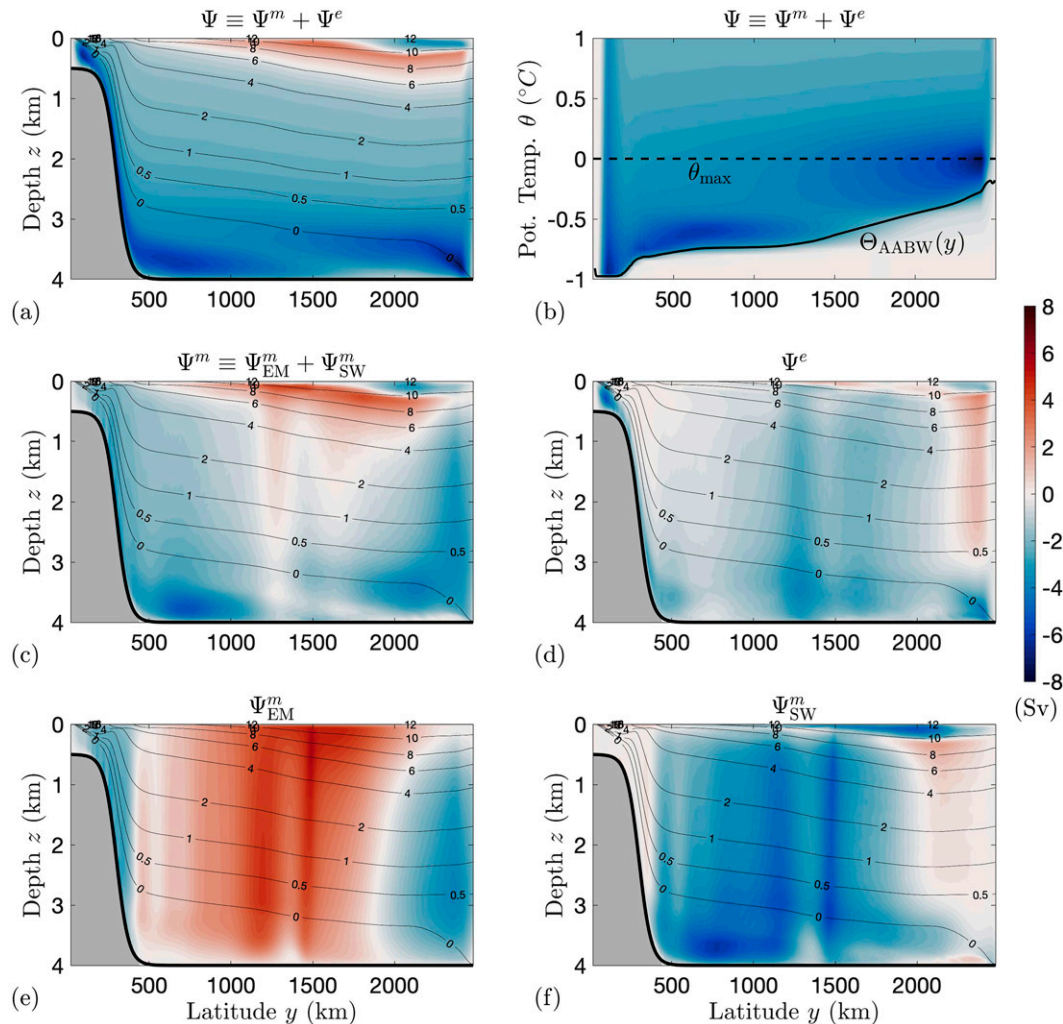


FIG. 4. Decomposition of the meridional overturning circulation in the reference simulation: (a) isopycnal overturning streamfunction (colors), calculated by integrating meridional fluxes within temperature surfaces and mapping approximately to y/z space, overlaid with time-/zonal-mean potential temperature ($^{\circ}\text{C}$; contours); (b) isopycnal overturning streamfunction (colors), plotted in potential temperature space across the $\theta < 1^{\circ}\text{C}$ layer, with AABW dynamically defined potential temperature bound $\theta_{\text{max}} = 0^{\circ}\text{C}$ (dashed line) and AABW transport-weighted potential temperature $\Theta_{\text{AABW}}(y)$ (solid line); (c) mean and (d) eddy overturning streamfunctions mapped to y/z space (colors) overlaid with and time-/zonal-mean potential temperature (contours); and (e) Eulerian mean and (f) standing wave overturning streamfunctions mapped to y/z space (colors) overlaid with time-/zonal-mean potential temperature (contours).

isopycnal overturning circulation of the reference case is characterized by northward flow along the continental shelf and across the sea floor, representing the export of AABW from its formation sites to abyssal ocean basins. For much of the middepth range, the flow is southward, with a northward flow near the surface in the northern portion of the domain. This two-cell circulation pattern is qualitatively consistent with observations and modeling of the Southern Ocean overturning, although the upper cell is somewhat shallower than observations (Lumpkin and Speer 2007; Marshall and Speer 2012; Talley 2013; Cessi 2019). The unrealistically shallow upper cell is likely a consequence of the fixed pattern of surface buoyancy fluxes and relatively small

isopycnal slopes (Marshall and Radko 2003). However, the shallow upper cell does not significantly affect our analysis of the overturning circulation as the focus of our study is the export of AABW. The strength of the lower cell is approximately 4 Sv, with localized peaks of 5–6 Sv. This agrees closely with the inverse model estimate of Lumpkin and Speer (2007), who estimated 4.9 ± 2.5 Sv of northward bottom water export in the Atlantic sector of the Southern Ocean at 62°S . Crudely scaling up the AABW export in the 4000-km-long channel based on the ~ 20000 -km length of a latitude circle in the Southern Ocean yields ~ 20 Sv, which falls in the middle of the range of previous estimates of the abyssal overturning cell strength (Cessi 2019).

The lower cell in the model is subdivided into two distinct recirculations: one subcell extending along the seafloor from the continental shelf to the middle of the domain (approximately $y = 1400$ km), with an overlying subcell occupying the northern portion of the abyss (see Figs. 4a,b). In the southern subcell, AABW is upwelled, and AABW downwells in the northern subcell. This feature is consistent with the bottom-intensified mixing in this model and its impact on the advective–diffusive balance (Munk 1966; Wunsch and Ferrari 2004; Ferrari et al. 2016) that drives entrainment into the AABW layer and thus necessitates an overturning structure with downwelling into the northern portion of the lower cell. Although there is inconclusive observational evidence to determine if such an AABW recirculation exists in nature, evidence of such a two-cell abyssal structure is present in prior modeling and reanalysis studies (Lumpkin and Speer 2007; Newsom et al. 2016; Cessi 2019; Kiss et al. 2020). Consequences of the two-cell abyssal circulation pattern on AABW transformation are discussed in further detail in section 4b.

Figures 4c and 4d show that the overturning is primarily supported by the time-mean flow, with the exception of the continental shelf/slope and the core of the ACC, where the eddy-driven overturning also contributes substantially. The time-mean overturning results from a near-compensation between the Eulerian-mean overturning, which closely resembles the wind-driven Ekman transport, and an opposing contribution from standing waves (Figs. 4e,f). Note that computing the streamfunctions via integration along mean streamlines, rather than meridians, would likely place greater emphasis on the transient eddy overturning (Marshall and Radko 2003; Abernathey and Cessi 2014).

To analyze lateral circulation of AABW, we must first define the AABW layer. A commonly used observational definition is that AABW consists of density classes that lie deeper than the Drake Passage, i.e., those that are not circumpolar (Talley 2011). This definition is unsuitable for the model used in this study because our experiments include cases in which the ACC is completely unobstructed by bathymetry. An alternative would be to use the 0°C isotherm as an upper bound for the AABW layer. In the model configuration, waters colder than 0°C can only exist in the interior at depth due to the buoyancy on the continental shelf, and at the surface within 100 km of the southern boundary (cf. Stewart and Thompson 2013). However, in some experiments the northward-flowing waters reach temperatures greater than 0°C by the time they reach the northern boundary. We therefore define a potential temperature bound for the AABW layer by selecting the temperature level coinciding with the minimum value of the isopycnal overturning streamfunction at the southern edge of the northern sponge layer ($y = 2400$ km). This definition corresponds to the temperature at the top of the northward-flowing AABW layer at the northern point of the domain. For most cases, this yields a potential temperature bound $\theta_{\max} = 0^{\circ}\text{C}$, with cases having varied topography or higher diffusivities having higher potential temperature boundaries. See Table 2 for a complete list of dynamically defined potential temperature bounds used for each experiment, and Fig. 4b for a visualization of θ_{\max} . Unless otherwise noted,

the “AABW layer” refers to all water within and below the density layer specified by the dynamically defined potential temperature bound for each specific model run.

To visualize circulation pathways within the AABW layer, we calculate a horizontal AABW quasi streamfunction χ_{AABW} . Under the assumption that the isopycnal heave and diapycnal velocity are negligibly small, the horizontal transport integrated over the AABW layer is approximately nondivergent:

$$\nabla \cdot \bar{\mathbf{U}}^t \approx 0, \quad \mathbf{U} = \int_{z=\eta_b}^{z=0} \mathbf{u}_h \mathcal{H}[\theta_{\max} - \tilde{\theta}(x, y, z, t)] dz, \quad (6)$$

where $\mathbf{u}_h = (u, v)$ denotes the horizontal velocity vector. We can then define a transport streamfunction for the flow within this layer that approximately satisfies

$$\bar{\mathbf{U}}^t \approx -\nabla \times \chi_{\text{AABW}} \hat{\mathbf{z}} \Rightarrow \chi_{\text{AABW}}(\mathbf{x}_h) \approx \int_{\mathbf{x}_h^0}^{\mathbf{x}_h} \bar{\mathbf{U}}^t \cdot \hat{\mathbf{n}} dl. \quad (7)$$

The rightmost expression in (7) defines the quasi streamfunction at a given horizontal location \mathbf{x}_h via a line integral from a reference horizontal location \mathbf{x}_h^0 , with $\hat{\mathbf{n}}$ denoting a unit vector normal to the path of integration.

While χ_{AABW} is calculated and plotted as an analog to a barotropic streamfunction, some caution is required in interpreting its streamlines. First, χ_{AABW} is nonperiodic, exhibiting a zonal jump from one boundary of the reentrant domain to the other. This is primarily due to the net northward transport within the AABW layer, which is balanced by southward flow in overlying layers. This net northward transport requires that χ_{AABW} increase from west to east across the domain, resulting in a “step” in the quasi-streamline transport at the zonal boundary; for example, if the net meridional transport at a given latitude is Ψ_0 , then a quasi streamline $\chi_{\text{AABW}} = \chi_0$ exiting through the eastern boundary will reenter from the western boundary as the quasi streamline $\chi_{\text{AABW}} = \chi_0 + \Psi_0$.

As stated in (6), the quasi streamfunction must be defined across a layer with zero isopycnal transport divergence to be mathematically well defined. Isopycnal heave makes a negligible contribution to the transport divergence; for the reference case, the isopycnal heave integrated from $500 \leq y \leq 2300$ km is 2.2% of the value of net northward transport in the AABW layer (not shown). Diapycnal transport, however, contributes more substantially to the nondivergence of the AABW flow. From $500 \leq y \leq 2300$ km, the diapycnal transport is about 44% of the value of net northward transport for the reference case, so the diapycnal transport is nonnegligible at the scale of the whole domain. Therefore, tracing flow pathways from one zonal boundary to the other is likely to incur substantial errors. However, in this study we primarily use the quasi streamfunction within 500 km of the meridional ridge, for the purposes of flow visualization and zonal transport calculation. Although there is a region of high diapycnal downwelling through the isotherm θ_{\max} in the lee of the topography (magnitude up to 10^{-5} m s^{-1} , not shown), the downwelling in the reentrant channel is less significant. In this region the diapycnal velocity is typically just a few percent of the net throughflow (not shown), so tracing flow pathways along

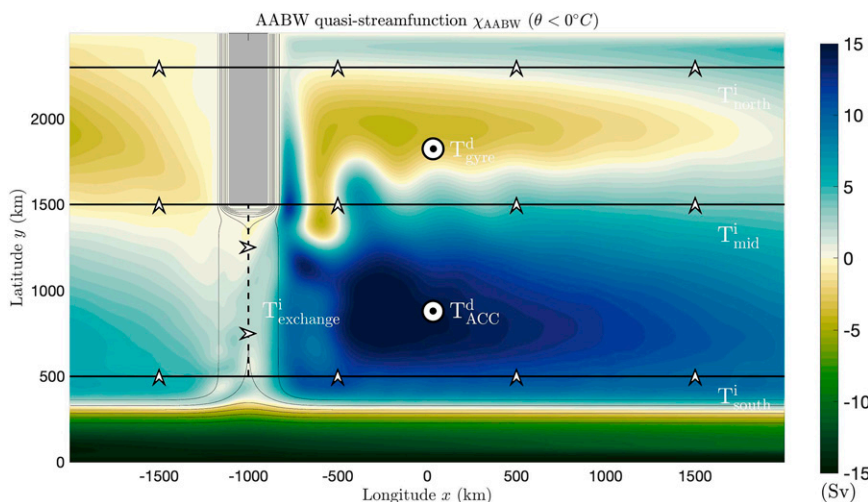


FIG. 5. Visualization of AABW circulation patterns and pathways for the reference simulation, where $\theta_{\max} = 0^\circ\text{C}$, showing the AABW quasi streamfunction χ_{AABW} (colors) with bathymetry (contours) with spacing of 500 m. The flow moves such that smaller values of χ_{AABW} are on the left. Black lines and arrows respectively indicate boundaries and directions of positive transport for our two-box model, discussed in section 4.

streamlines of χ_{AABW} across the ridge incurs relatively small errors. To minimize these errors, we have selected an integration scheme for χ_{AABW} to avoid areas of high diapycnal velocity in the northern and southern sponge regions. We compute χ_{AABW} using (7), defining $\chi_{\text{AABW}} = 0$ along the northern boundary and along the margins of the northern continent. We first compute χ_{AABW} at all latitudes within the longitude band $900 \leq x \leq 1100$ km by integrating southward from the continental margin. We then integrate directly eastward to compute χ_{AABW} at all latitudes within the longitude range $x > 1100$ km and directly westward to compute χ_{AABW} at all latitudes within the longitude range $x < 900$ km.

In Fig. 5 we illustrate the typical horizontal circulation patterns within the AABW layer in the model via the AABW quasi streamfunction for the reference simulation. Note that χ_{AABW} is nonperiodic, exhibiting a jump at the zonal boundaries of the model domain, due to the net northward transport within the AABW layer. The AABW circulation is dominated by gyres: a cyclonic circulation centered at approximately $y = 1000$ km, qualitatively resembling the subpolar gyres in the Ross and Weddell Seas (Orsi et al. 1993; Wilson et al. 2022), and an anticyclonic circulation centered at approximately $y = 2000$ km, corresponding to a subtropical gyre (Pedlosky 1990). The western edge of the southern gyre consists of a northward-flowing deep western boundary current (DWBC) along the eastern side of the ridge, analogous to the deep AABW boundary currents identified in previous studies (Fukumachi et al. 2010; Kusahara et al. 2017; Foppert et al. 2021). Some of the quasi streamlines from the DWBC appear to extend to the northern boundary, suggesting that this is a major pathway for the northward export of AABW.

In addition to the northward flow in the DWBC, the quasi streamlines crossing the meridional ridge ($x = -1000$ km) indicate that there is some interbasin exchange of AABW

(cf. van Seville et al. 2013). For the reference-case simulation, there is approximately 2 Sv of interbasin AABW exchange across the meridional ridge, using the 0°C isotherm as the upper boundary for the AABW layer. Previous estimates of AABW transport between basins vary widely: for example, AABW may be defined as water masses that are too deep to cross Drake Passage (Talley 2011). In contrast Cessi (2019) computed a transport of 18.9 Sv through Drake Passage at potential densities greater than 37.52 kg m^{-3} (referenced to 2100 dbar).

3. Controls on meridional versus zonal transport of AABW

In this section, we outline the controls on the “bulk” transport of AABW, i.e., integrated across the entire AABW layer. In section 4 we examine how these transports vary as a function of density within the AABW layer and relate them to water-mass transformation.

a. Overturning circulation

We first examine the strength of the zonally integrated overturning circulation, as this provides a necessary reference point for the “interbasin” transport. In Figs. 6a, 6c, 6e, and 6g, we visualize the strength and structure of the overturning circulation for a range of experiments with varying ridge height, which we find to be a key control on this circulation. Each simulation exhibits a similar circulation structure, with a shallow clockwise upper cell overlying a counterclockwise lower cell extending through the majority of the ocean’s interior to the seafloor. The upper cell becomes shallower for cases with higher ridges, with the lower cell occupying a greater volume. The strength of the overturning circulation in the lower cell is only slightly enhanced from the no-ridge case to the case

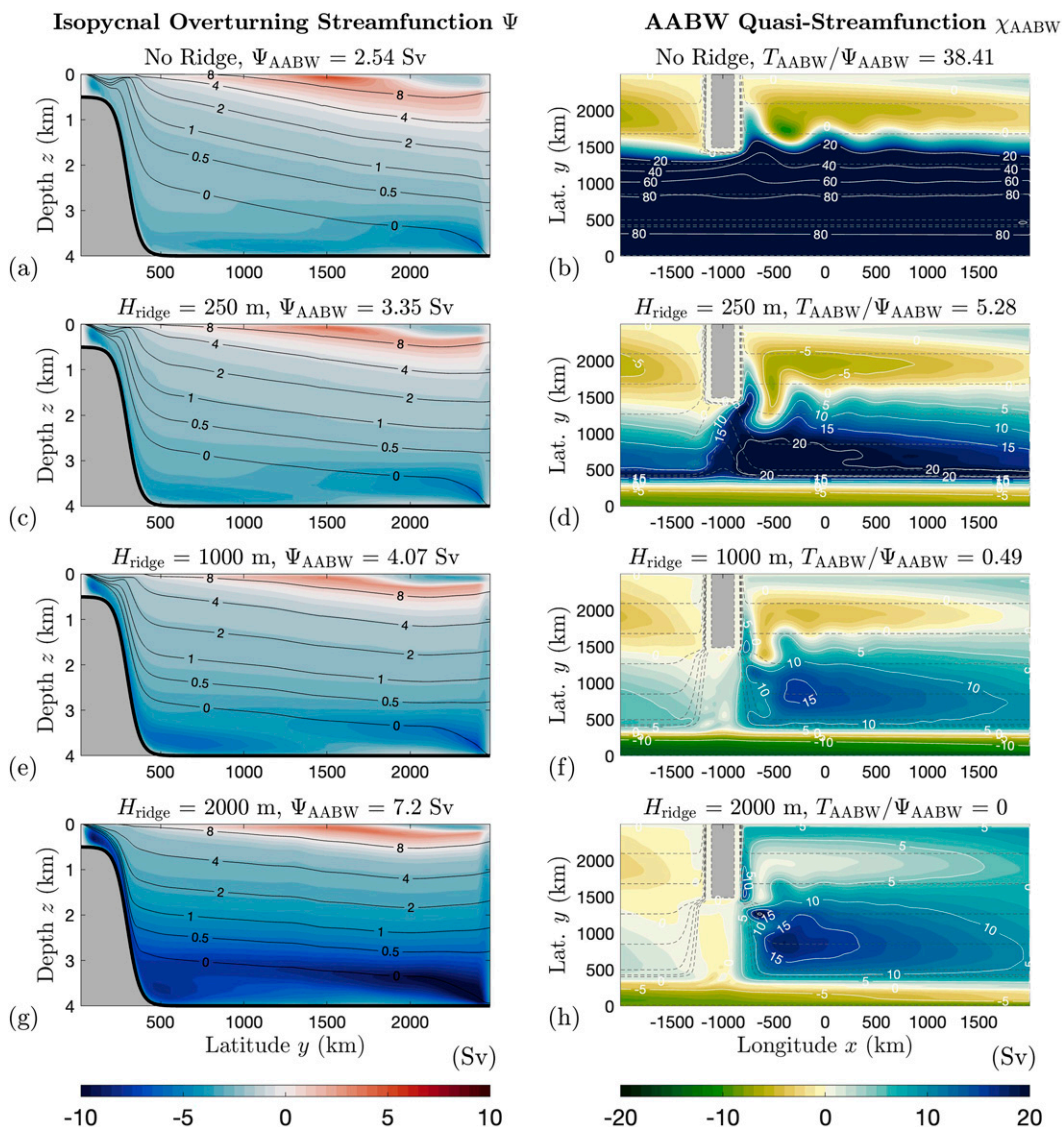


FIG. 6. A comparison of meridional overturning circulation and AABW layer ($\theta < 0^\circ\text{C}$) circulation between model experiments with no ridge and 250-, 1000-, and 2000-m ridges. Ridge height and corresponding transport parameters are noted in the panel titles. (a),(c),(e),(g) Isopycnal overturning streamfunction (colors), and zonal/time-mean potential temperature surfaces (contours). (b),(d),(f),(h) AABW quasi streamfunction defined over the $\theta < 0^\circ\text{C}$ layer (colors) with highlighted quasi streamlines (white contours) and lines of constant planetary potential vorticity f/H (dashed gray contours), where f is the Coriolis parameter and H is depth.

with $H_{\text{ridge}} = 250$, shown in Figs. 6a and 6c, respectively. However, this strength significantly increases from the cases with $H_{\text{ridge}} \leq 250$ m when compared with the cases with $H_{\text{ridge}} \geq 1000$ m, shown in Figs. 6a, 6c, 6e, and 6g, respectively, with the case of $H_{\text{ridge}} = 2000$ m displaying the strongest overturning circulation in the lower cell.

The structure of the two subcell abyssal circulation is also modulated by the height of the ridge. For higher ridges, the northern subcell occupies a greater latitudinal extent of the domain; in the case of $H_{\text{ridge}} = 2000$ m, the northern subcell almost entirely subsumes the southern subcell. The latitudinal extent of the subcells is also affected by magnitude of the

diapycnal diffusivity (not shown) with higher diffusivity associated with an expanded, stronger southern subcell and a contracted, weaker northern subcell, which is explained by the advective–diffusive balance.

In Fig. 7, we examine the sensitivity of diagnostics of the abyssal overturning circulation strength and isopycnal structure across the entire suite of experiments. We plot each diagnostic as a function of ridge height, because we find that the ridge height explains most of the variation between experiments. The dependencies upon other parameters are indicated via differing marker styles. Figure 7a surveys the sensitivity of AABW meridional export, and is defined using

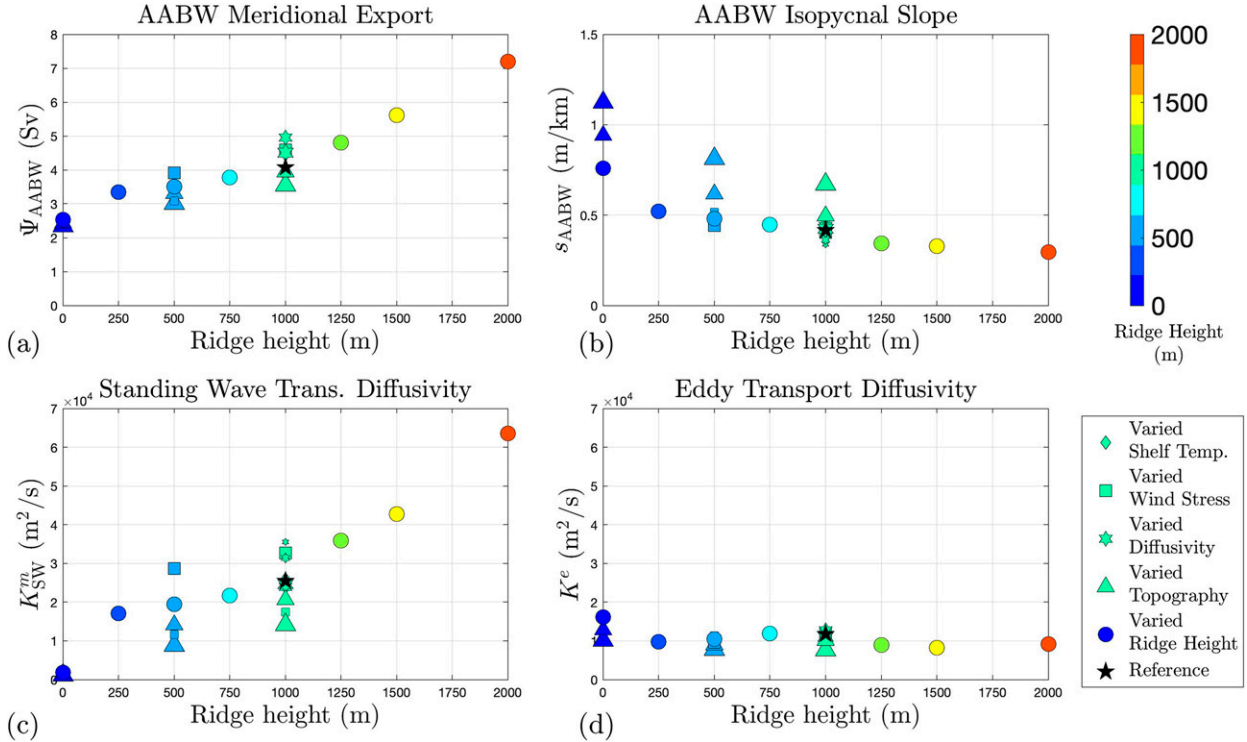


FIG. 7. Sensitivity of key overturning circulation diagnostics to ridge height (symbol color) and other model parameters (symbol style). Relative size differences within symbol styles indicate relative parameter variations. For all sensitivity figures, the reference-case simulation is represented by a black star. (a) Meridional export of AABW computed from the isopycnal overturning streamfunction via (8). (b) Isopycnal slope at dynamically defined potential temperature bound of AABW layer, computed via (10). Transport diffusivities estimated from (c) standing wave and (d) transient eddy components of the flow via (11) and (12), respectively.

a min–max method following Stewart and Thompson (2013) as

$$\Psi_{\text{AABW}} = \max_{L_{\text{sponge}} < y < L_y - L_{\text{sponge}}} [\min_{\theta}(\Psi)]. \quad (8)$$

By first finding the minima (i.e., the most negative values) of the streamfunction in potential temperature space, we obtain the greatest northward transport at each latitude. Then, by taking the maximum (i.e., the least negative value) of these minima, we obtain the magnitude of northward transport that crosses the entire specified latitude band. In this way, this diagnostic approximately quantifies the transport associated with the greatest continuous streamline from the southern boundary to the northern boundary. AABW export values for the suite of simulations range from 2.5 to 7.2 Sv, with the reference case yielding a value of 4.1 Sv. We find that AABW meridional export scales approximately linearly with ridge height in the model, with other parameter perturbations producing relatively small changes. From the case with $H_{\text{ridge}} = 0$ m to $H_{\text{ridge}} = 2000$ m, the model displays nearly a threefold increase in the magnitude of AABW export. Therefore, across the parameter space explored here, the height of the meridional ridge exerts the strongest control on the abyssal overturning strength.

The export of AABW is closely linked to the slope of isopycnals across the ACC (e.g., Ito and Marshall 2008; Nikurashin and Vallis 2011; Stewart and Thompson 2013). Furthermore, in

section 3b we show that the thickness of the AABW layer in the ACC plays a key role in determining its interbasin transport. Thus, to elucidate the sensitivity of the overturning circulation to the ridge height, in Fig. 7b we plot the sensitivity of the isopycnal slope of AABW layer to the model control parameters. We define the AABW layer thickness below $\theta = \theta_{\text{max}}$ as

$$h_{\text{AABW}} = \int_{z=\eta_b}^{z=0} \mathcal{H}[\theta_{\text{max}} - \tilde{\theta}(x, y, z, t)] dz. \quad (9)$$

We then compute the AABW isopycnal slope, s_{AABW} , as the meridional gradient of h_{AABW} , averaged across the latitude band of the ACC; that is,

$$s_{\text{AABW}} = \frac{\Delta \overline{h_{\text{AABW}}}^{x,d}}{\Delta y}, \quad (10)$$

where Δ denotes meridional differences between $y = 500$ km and 1500 km. In Figs. 6a, 6c, 6e, and 6g, the 0°C isotherm visualizes the slope of this isopycnal for each simulation. Consistent with observations of AABW volumes across the global ocean, the thickness of the AABW layer decreases from south to north in the model (Johnson 2008). Cases with low or no meridional ridge exhibit steeper AABW isopycnal slopes than cases with higher meridional ridges. This aligns with the findings of Stewart and Hogg (2017), who found that a

meridional bump, blocking only a portion of the reentrant ACC channel, was associated with steeper isopycnal slopes when compared with cases with a meridional ridge. Cases with higher random topography are associated with further steepening of AABW isopycnal slopes.

To interpret the sensitivity of the AABW export and isopycnal slope to bathymetric perturbations, we quantify the efficiency of both standing waves/meanders and transient eddies (see Fig. 4) in transporting AABW northward across the ACC. Specifically, we define bulk transport diffusivities for the standing wave and transient eddy components of the flow as the ratio of the meridionally averaged northward transport below $\theta = \theta_{\max}$ to the isopycnal thickness gradient:

$$K_{\text{SW}}^m = \frac{1}{L_x s_{\text{AABW}} \Delta y} \int_{y=500\text{km}}^{y=1500\text{km}} \Psi_{\text{SW}}^m|_{\theta=\theta_{\max}} dy \quad \text{and} \quad (11)$$

$$K^e = \frac{1}{L_x s_{\text{AABW}} \Delta y} \int_{y=500\text{km}}^{y=1500\text{km}} \Psi^e|_{\theta=\theta_{\max}} dy. \quad (12)$$

Figures 7c and 7d show the sensitivity of these diffusivities to the model control parameters. The transient eddy diffusivity is largely insensitive to the ridge height, remaining close to $K^e = 1000 \text{ m}^2 \text{ s}^{-1}$ across all of the model simulations, except for the no-ridge case where K^e is roughly $\sim 60\%$ greater. This indicates the importance of eddies in the northward transport of AABW for cases lacking a meridional barrier. In contrast, the standing wave transport diffusivity increases approximately linearly with the ridge height, increasing the combined transport diffusivity ($K_{\text{SW}}^m + K^e$) by a factor of ~ 5 from no ridge to $H_{\text{ridge}} = 2000 \text{ m}$. Thus, the dramatic increase in standing wave transport efficiency appears to be primarily responsible for the increase in net AABW export and reduction in AABW isopycnal slope (Figs. 7a,b). In contrast, the inclusion of random topography reduces the transport diffusivities by as much as a factor of 2, leading to substantially ($\sim 50\%$) steeper AABW isopycnal slopes and slightly ($\sim 10\%$ – 20%) reduced AABW export. This is consistent with the finding of Jouanno and Capet (2020) that random topography suppresses the mesoscale eddy field, which in turn may be expected to reduce the effective transport diffusivity due to standing waves (Abernathey and Cessi 2014) by reducing buoyancy transport in both the eddy and standing wave components of the flow.

b. Horizontal AABW circulation and interbasin exchange

We now discuss the interbasin transport of AABW, that is, transport of AABW across the meridional ridge, using the meridional transport of AABW as a reference point for each of the simulations. Figures 6b, 6d, 6f, and 6h show the AABW quasi streamfunction for each run. The overall structure of horizontal circulation visually exhibits substantial changes in response to variations in the ridge height. In the no-ridge case shown in Fig. 6b, zonally reentrant quasi streamlines occupy the majority of the ACC latitude band, supporting a relatively large flux ($\geq 60 \text{ Sv}$) of AABW between basins. Note the northward meander of the reentrant quasi streamlines in the

lee of the topography (located approximately at $x = -500 \text{ km}$), indicating a northward excursion of the ACC, as well as a gyre recirculation in the northern portion of the basin (located approximately at $y \geq 1500 \text{ km}$). Introducing even a 250-m-high ridge (Fig. 6d) changes this structure dramatically: although the model still exhibits reentrant quasi streamlines that transport AABW between basins, the magnitude of this exchange is greatly reduced ($\leq 15 \text{ Sv}$) and the quasi streamlines follow a much more exaggerated northward meander in the lee of the topography. Furthermore, a gyre recirculation of AABW appears in the latitude band of the ACC, situated in the lee of the ridge (Wilson et al. 2022). Further increasing the ridge height to $H_{\text{ridge}} = 1000 \text{ m}$ (Fig. 6f) reduces the interbasin exchange to $\leq 0.5 \text{ Sv}$ and strengthens the AABW recirculation in the latitudes of the ACC. As in Patmore et al. (2019), the strength of this subpolar gyre is strongly influenced by the height of the meridional ridge, supporting a DWBC along the lee side of the ridge and topography that provides a direct northward route for AABW. Raising the ridge to $H_{\text{ridge}} = 2000 \text{ m}$ shuts down the interbasin exchange entirely. The DWBC strengthens further relative to the case of $H_{\text{ridge}} = 1000 \text{ m}$, with almost all of the AABW being exported directly northward via this route (cf. Figs. 7c,d).

We quantify the magnitude of interbasin transport in each model run, T_{AABW} , as the transport associated with all quasi streamlines of χ_{AABW} that cross the meridional ridge. We define this quantity in a manner similar to Ψ_{AABW} in (8), namely, using a min–max method to compute T_{AABW} as

$$T_{\text{AABW}} = \min_{X_{\text{ridge}} - W_{\text{ridge}}/2 \leq x \leq X_{\text{ridge}} + W_{\text{ridge}}/2} [\max_y (\chi_{\text{AABW}})]. \quad (13)$$

Here, we solve for the greatest horizontal transport at each longitude, and then take the minimum of these values to obtain the horizontal transport that crosses the entire zonal extent of the meridional ridge. This method approximately yields the greatest continuous quasi streamline from one side of the ridge to the other. To compare the interbasin transport between the model simulations, we normalize it by the northward export of AABW, defining the bulk AABW “transport ratio” as

$$R_{\text{AABW}}^i = \frac{T_{\text{AABW}}}{\Psi_{\text{AABW}}}. \quad (14)$$

This ratio quantifies the fraction of the AABW that is transported across the ridge (i.e., between “basins”) as it crosses the ACC. The transport ratio can also be conceptualized as the approximate number of “loops” around the model ACC completed by the average parcel of AABW as it flows northward. In other words, R_{AABW}^i quantifies how close the simulated flow lies to the conduit and blender extremes depicted in Fig. 2.

Figures 8a–d show the sensitivity of the AABW transport ratio to several of the model control parameters, selected because they exhibit the strongest influence on this transport, and to the total zonal transport of the ACC across the ridge. We include only the key sensitivities of the AABW transport ratio here; the transport ratio did not display any notable

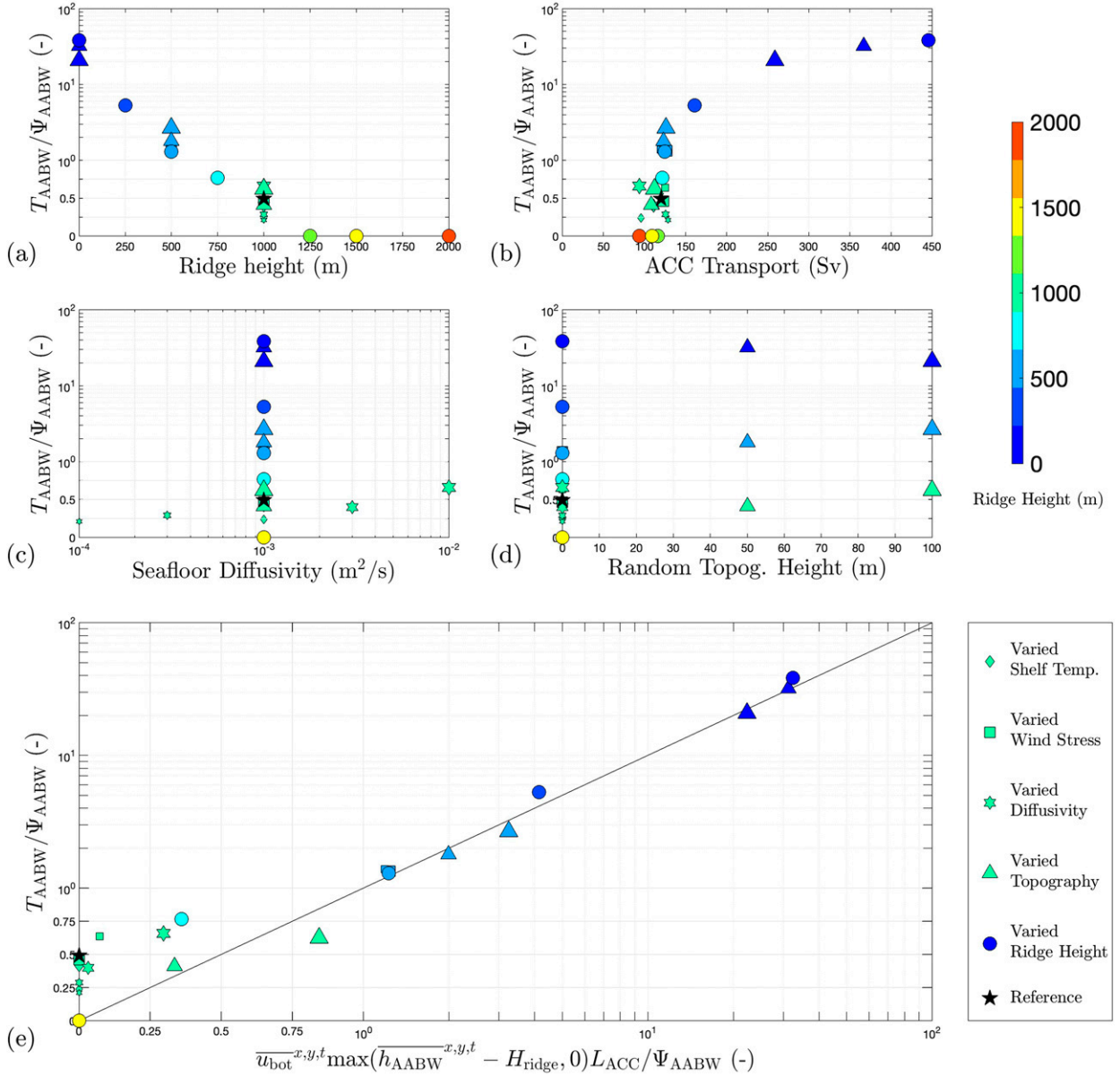


FIG. 8. Sensitivity of AABW transport ratio to ridge height (symbol color) and other model parameters (symbol style), plotted as a function of (a) ridge height (m), (b) ACC transport (Sv), (c) maximum diffusivity at the seafloor ($\text{m}^2 \text{s}^{-1}$), and (d) RMS random topography height (m). The transport ratio axis is linear for ratios from 0 to 1 and logarithmic for all transport ratios >1 . (e) A simplified equation for the AABW transport ratio based on passive advection of AABW over the ridge by the bottom velocity u_{bot} of the ACC. Note the nonlinear axis ranges, which are used to span the very large range of transport ratios while preserving cases in which the transport ratio is zero.

dependence on wind stress or AABW shelf temperature. The strongest dependency of the AABW transport ratio was upon ridge height, shown in Fig. 8a. As indicated by our qualitative discussion of AABW circulation patterns and ridge height, higher ridges are associated with a restriction of interbasin exchange, yielding lower transport ratios. For low-ridge cases (≤ 250 m) we find that the AABW transport ratio scales approximately linearly with overall ACC transport, as shown in Fig. 8b. This suggests that AABW is largely passively advected over the ridge by the deep-reaching flow of the ACC.

Varying the maximum seafloor diffusivity (Fig. 8c) leads to a modest increase in the transport ratio, from ~ 0.21 to ~ 0.65 as κ_{max} increases from 10^{-4} to $10^{-2} \text{ m}^2 \text{s}^{-1}$. A possible mechanism for this dependence is that higher diffusivities mix the AABW layer across a greater vertical extent in the water column, rendering it more likely to be transported across the meridional ridge. Varying the height of the random topographic bumps (Fig. 8d) generally leads to modest changes in the transport ratio. The strongest sensitivity to random topography occurs when the meridional ridge height is zero, with

higher random topography being associated with lower AABW transport ratios. This is likely because the random topography is associated with a reduction in total ACC transport, and thus impedes the zonal advection of AABW by the ACC.

The strong dependence of the AABW transport ratio on the ridge height and ACC transport (Figs. 8a–d) suggests that AABW is passively advected over the ridge by the deep-reaching component of the ACC flow. To test this hypothesis, we formulate a simplified equation for the interbasin AABW transport, relating T_{AABW} to the ridge height, AABW layer thickness, and bottom velocity in the ACC:

$$T_{\text{AABW}} \sim \overline{u_{\text{bot}}}^{x,y,t} [\max(\overline{h_{\text{AABW}}}^{x,y,t} - H_{\text{ridge}}, 0)] L_{\text{ACC}}. \quad (15)$$

Here $L_{\text{ACC}} = 1000$ km is the meridional width of the ACC over the ridge, and u_{bot} denotes the ACC's zonal velocity at the sea floor, averaged across the longitude band of Drake Passage, $-1100 \leq x \leq -900$ km. We define the AABW layer thickness, h_{AABW} , as the elevation of the θ_{max} isopycnal. To estimate T_{AABW} via (15) we compute the average the sea floor velocity and AABW layer thickness within the latitude band of the ACC ($500 \leq y \leq 1500$ km). For cases where the height of the meridional ridge exceeds the thickness of the AABW layer [and thus $\max(\overline{h_{\text{AABW}}}^{x,y,t} - H_{\text{ridge}}, 0) = 0$], T_{AABW} is predicted to be zero. To compare the diagnosed AABW transport ratio with that predicted by (15), we divide by the diagnosed AABW export, Ψ_{AABW} :

$$R_{\text{AABW}}^i \sim \frac{\overline{u_{\text{bot}}}^{x,y,t} [\max(\overline{h_{\text{AABW}}}^{x,y,t} - H_{\text{ridge}}, 0)] L_{\text{ACC}}}{\Psi_{\text{AABW}}}. \quad (16)$$

We could alternatively have posed a scaling for Ψ_{AABW} , for example, assuming a linear dependence of Ψ_{AABW} on H_{ridge} , as suggested by Fig. 4a. However, it is unclear whether such a relationship would generalize if the AABW formation processes on the continental shelf were more realistically represented, e.g., including both restoring and fixed buoyancy fluxes (Stewart et al. 2014).

Figure 8e evaluates our simplified (15) against the diagnosed AABW transport ratio. The simplified equation holds well for high AABW transport ratios (i.e., for relatively low ridges with relatively large ACC transports) but underpredicts the transport ratio for intermediate ridge heights of $750 \leq H_{\text{ridge}} \leq 1000$ m. This indicates that AABW is indeed passively advected between basins for ridge heights satisfying $H_{\text{ridge}} \ll h_{\text{AABW}}$, and is consistently obstructed for $H_{\text{ridge}} \gg h_{\text{AABW}}$. However, for $H_{\text{ridge}} \approx h_{\text{AABW}}$ the dynamics of the interbasin transport are more complicated than the passive advection over the ridge assumed in (15).

4. Density-resolved AABW transport and transformation

Thus far, we have examined metrics that describe the AABW as a single, bulk layer, without taking into account any density-dependent structure that may be present. In the reference simulation, for example, we have defined the AABW layer to encompass the waters extending from -1°C , the reference imposed AABW formation temperature on the

shelf, to 0°C , the dynamically defined potential temperature bound for this model run. This range of densities encompasses roughly the deepest 1000 m of the domain for the reference case. It is possible that different density classes within the AABW layer are subject to varying degrees of interbasin exchange: for example, we might expect the densest AABW to be more likely to cross the ACC via conduits (see Fig. 2 and Kushara et al. 2017). In this section we take a density-resolved view of the meridional versus zonal transport of AABW, utilizing the water-mass transformation framework (Groeskamp et al. 2019).

a. Density-resolved transport diagnostics

To examine relevant transports as a function of density, we define a two-box budget across the model domain, with zonal and meridional boundaries chosen to highlight the distinct circulation regimes in different regions of the domain. We note that our definition is one of many approaches that could have been taken; for example, similar analysis could be carried out by defining boundaries using dynamical features of the flow, such as streamlines.

The two-box budget is visualized in Fig. 5 with solid black lines as boundaries, and white arrows indicating the direction of positive transport across each boundary. For the box centered around the ACC, we have set the zonal boundaries extending from just beyond the northern edge of the shelf ($y = y_{\text{south}} = 500$ km) to the southern extent of the topography ($y = y_{\text{mid}} = 1500$ km). This encompasses the latitude band of the ACC, which lacks meridional boundaries and thus allows zonal recirculation, while avoiding the westward flows along the southern continental shelf and slope. We have also set a meridional boundary along the spine of the meridional ridge ($x = -1000$ km), indicated by the dashed vertical line in Fig. 5. The second box in our two-box budget includes the northern basin of the model domain, where zonal flow is obstructed by the “continent” centered at $x = -1000$ km. For most of the simulations, an anticyclonic gyre circulation develops here. For the gyre box, we have set the zonal boundaries extending from the southern extent of the topography ($y = y_{\text{mid}}$) to just south of the northern sponge layer ($y = y_{\text{north}} = 2300$ km) to avoid artificial effects from the restoring layer.

Across each of these zonal boundaries (solid lines in Fig. 5), we calculate the zonally integrated meridional transport as a function of potential temperature. We first define a θ -dependent analog of the volume transport integrated over the AABW layer [(6)],

$$U_\theta = \int_{z=\eta_b}^{z=0} \mathbf{u}_h \mathcal{A}[\theta - \tilde{\theta}(x, y, z, t)] dz. \quad (17)$$

For our calculation of the isopycnal transport across the southernmost boundary, T_{south}^i , we calculate the net northward transport below each isotherm θ :

$$T_{\text{south}}^i(\theta) = \oint_{y=y_{\text{south}}} \overline{V}_\theta^i dx. \quad (18)$$

Similarly, to calculate T_{mid}^i and T_{north}^i , we set $y = y_{\text{mid}}$ and $y = y_{\text{north}}$ in (18), respectively.

For our calculation of the zonal exchange in the ACC box of our two-box budget, we take a similar approach as adopted in section 3. For each density level, we define a quasi streamfunction with an upper bound of integration corresponding to the specified potential temperature bound,

$$\chi_\theta(\mathbf{x}_h) = \int_{\mathbf{x}_h^0}^{\mathbf{x}_h} \bar{\mathbf{U}}_\theta^t \cdot \hat{\mathbf{n}} \, dl, \quad (19)$$

where the paths of integration in (19) are defined as described in section 2. Similar to our definition of the AABW quasi streamfunction (7), these quasi streamfunctions approximate the horizontal circulation below each isotherm θ . To determine the magnitude of interbasin exchange that occurs below this specified isotherm, we employ a “min–max” method on each quasi streamfunction, which quantifies the range of quasi streamlines that entirely cross the ridge:

$$T_{\text{exchange}}^i(\theta) = \min_{X_{\text{ridge}} - W_{\text{ridge}}/2 \leq x \leq X_{\text{ridge}} + W_{\text{ridge}}/2} [\max_y(\chi_\theta)]. \quad (20)$$

Note that this is analogous to (13).

Last, we calculate diapycnal transports through each isopycnal surface bounded by our boxes. For example, for the diapycnal transport through ACC box (T_{ACC}^d), we calculate

$$T_{\text{ACC}}^d(\theta) = \oint dx \int_{y_{\text{south}}}^{y_{\text{mid}}} dy \bar{\omega}_\theta^t. \quad (21)$$

Here $\bar{\omega}_\theta^t$ is the time-averaged diapycnal velocity, which we calculate as the divergence of the isopycnal velocity,

$$\bar{\omega}_\theta^t \approx -\nabla \cdot \bar{\mathbf{U}}_\theta^t. \quad (22)$$

Equation (22) holds under a sufficiently long time-average, such that the temporal drift in the elevation of the isotherm θ contributes negligibly to the volume budget. We calculate the diapycnal transport through gyre box, T_{gyre}^d , similarly.

Note that our two-box budget approximately conserves volume. That is, for a specified density level, the difference between isopycnal transports at two meridional transects is nearly equal to the diapycnal transport between them, with small variations due to isopycnal heaving of the layer. In particular,

$$T_{\text{south}}^i(\theta) - T_{\text{mid}}^i(\theta) \approx T_{\text{ACC}}^d(\theta) \quad \text{and} \quad (23)$$

$$T_{\text{mid}}^i(\theta) - T_{\text{north}}^i(\theta) \approx T_{\text{gyre}}^d(\theta). \quad (24)$$

This further implies that

$$T_{\text{south}}^i(\theta) - T_{\text{north}}^i(\theta) \approx T_{\text{ACC}}^d(\theta) + T_{\text{gyre}}^d(\theta). \quad (25)$$

These quantities enable us to define a pair of relevant transport ratios as a function of density. For our analysis in section 3, we defined a transport ratio for a bulk AABW layer by scaling the magnitude of the interbasin AABW exchange T_{AABW} by the magnitude of the overturning AABW export

Ψ_{AABW} . Similarly, we define a density-resolved version of the transport ratio as

$$R^i(\theta) = T_{\text{exchange}}^i / T_{\text{mid}}^i. \quad (26)$$

This allows us to examine, for each simulation, how the degree of dense water exchange across the ridge varies with density.

To examine the extent of diapycnal transformation experienced by different densities across the domain, we define a transformation ratio by scaling the total diapycnal transport by the isopycnal transport at the southernmost boundary of the two-box model. We define transformation ratio as

$$R^d(\theta) = \frac{T_{\text{ACC}}^d + T_{\text{gyre}}^d}{T_{\text{south}}^i}. \quad (27)$$

A transformation ratio of $R^d = 1$ indicates that all waters beneath that density class are entrained into lighter densities. A transformation ratio $R^d < 0$ indicates creation of water beneath that density class, and $R^d = -1$ represents a diapycnal transport into the layer that is equal in magnitude to the northward isopycnal transport at the southern boundary of the two-box model, T_{south}^i .

b. Density-resolved transport sensitivity

Figure 9 shows density-resolved transports and transport ratios for a selection of experiments with varying sea floor diffusivity and ridge height. We selected these experiments because variations in the diffusivity and ridge height lead to much larger changes in density-resolved transport diagnostics than do variations in the other model control parameters. In all panels, the reference case is represented by a solid black line, which we will examine first. Figure 9a shows the interbasin zonal exchange as a function of density. For the reference case, the potential temperature level of the first nonzero zonal exchange is -0.45°C , meaning all waters beneath this isopycnal are not exchanged between basins. The zonal exchange is a monotonically increasing function of density, indicating that the zonal transport beneath the 1°C isopycnal is eastward. Figures 9b–d show the meridional transport as a function of density across the southern, middle, and northern boundaries, respectively. For the reference case, we can see that the density structure of the meridional transport takes a similar form at each latitude: transport in the densest layers nearest the seafloor is northward, with the overlying waters flowing southward. The depth-integrated maximum northward transport from the seafloor is located at progressively warmer potential temperature levels, occurring at -0.70°C at the southern boundary, -0.15°C at the middle boundary, and -0.05°C at the northern boundary, which is consistent with the gradual warming of AABW as it progresses northward.

Figures 9e and 9f show the diapycnal transport as a function of density in the ACC and gyre boxes, respectively. The density dependence of the diapycnal transport is qualitatively similar across both boxes in the reference simulation. The densest waters near the seafloor have a positive diapycnal transport that increases with density, indicating upwelling

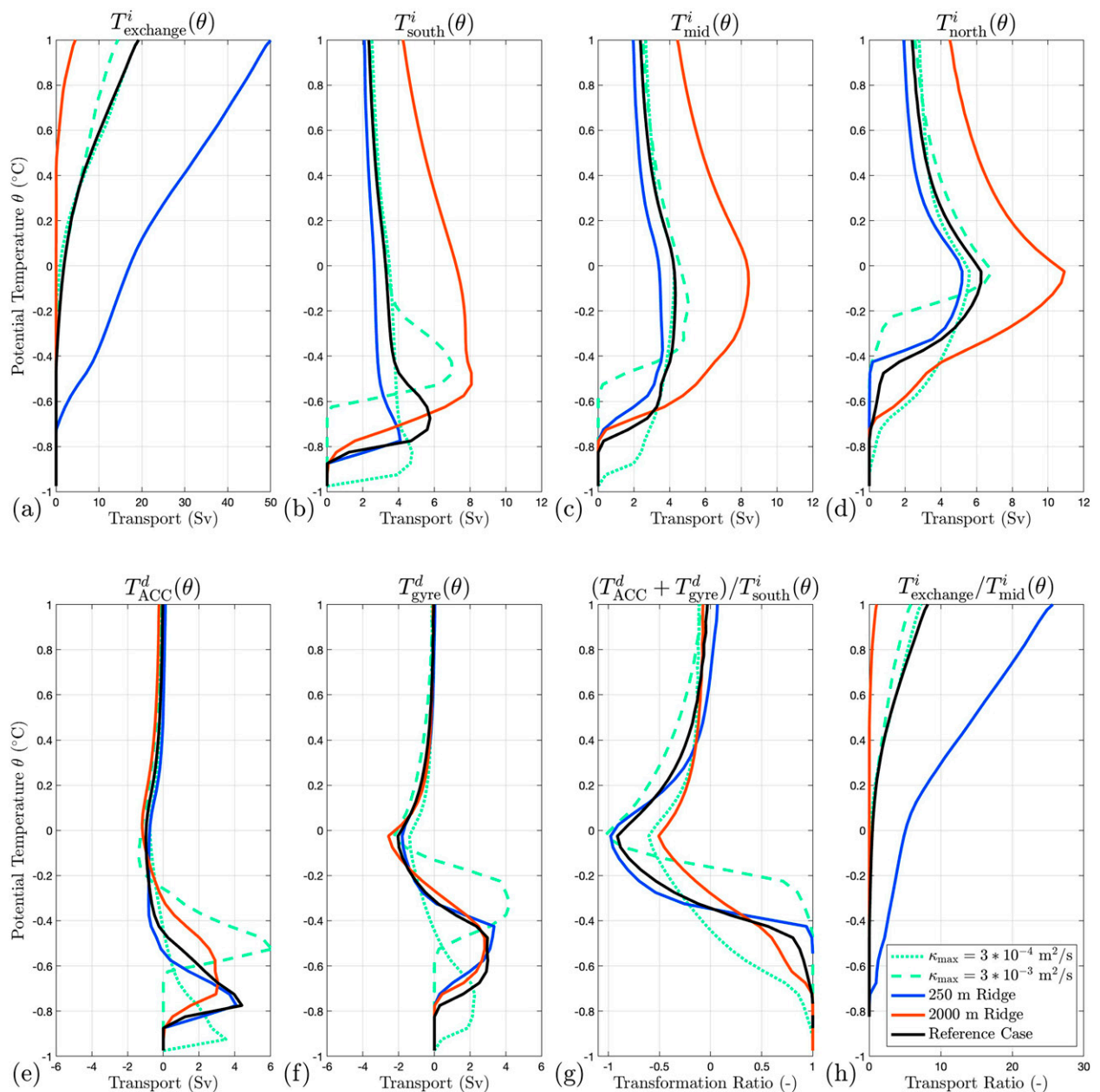


FIG. 9. Density-resolved transports and transport ratios for selected simulations, as a function of potential temperature ($^{\circ}\text{C}$): (a) zonal interbasin exchange, calculated via (20); isopycnal transport (Sv) across the (b) southern, (c) middle, and (d) northern meridional boundaries of our two-box budget; diapycnal transport (Sv) across the upper isopycnal surface of the (e) box ACC and (f) gyre boxes (see Fig. 5); (g) transformation ratio, calculated via (27); and (h) transport ratio, calculated via (26).

across the isopycnal and destruction of denser waters below. Above the potential temperature level of the maximum diapycnal upwelling, diapycnal transport decreases with density, indicating creation of waters in this density range. At sufficiently low densities the diapycnal velocity switches sign, indicating downwelling or entrainment into denser layers, until it reaches a maximum diapycnal downwelling at $\theta \approx 0^{\circ}\text{C}$. The destruction of dense waters occurs over a somewhat lower temperature range in the ACC box ($-0.85^{\circ} \leq \theta \leq -0.7^{\circ}\text{C}$)

than in the gyre box, ($-0.8^{\circ} \leq \theta \leq -0.55^{\circ}\text{C}$), which is consistent with observed abyssal two subcell circulation in the model. For the reference case, the boundary between the southern and northern abyssal subcells nearly aligns with y_{mid} , and thus T_{ACC}^d and T_{gyre}^d are representative of diapycnal transport in the southern and northern subcells, respectively. As visualized in Fig. 6c, the southern subcell occupies a narrower vertical extent in the domain, corresponding to a diapycnal transport, T_{ACC}^d , that is compressed toward a lower temperature range.

Figures 9g and 9h show the transformation ratio and the transport ratio, respectively, as a function of density. For the reference case, we see that the transformation ratio for the densest of waters along the seafloor is equal to 1, indicating that all waters that enter the boxes at the southern boundary beneath that isopycnal are upwelled or entrained into lighter density classes; that is, none of this water escapes through the northern boundary of the boxes. The transformation ratio decreases with density from the seafloor, indicating relatively less upwelling, reaching a minimum value at $\theta = -0.05^\circ\text{C}$. This potential temperature level corresponds to the greatest degree of entrainment into the layer (Figs. 9g,h); above this level, the transformation ratio increases back toward 0. The profile of the transport ratio for the reference case is a monotonically increasing function of density, indicating that the densest classes of water are exchanged the least and the lighter waters are exchanged more readily between basins and over the ridge. Thus, the shielding effect of the meridional ridge is most effective for the densest classes of bottom water.

For cases with varying ridge height, the model exhibits several key differences relative to the reference case. In particular, the overall magnitude of isopycnal transports is modulated by ridge height. Figure 9a shows that interbasin exchanges are larger for smaller ridges, with the 250-m ridge case having more exchange than the 1000-m reference case, and considerably more exchange than the 2000-m ridge case. Furthermore, there is nonzero interbasin exchange for $\theta > -0.750^\circ\text{C}$ in the 250-m ridge case, contrasting sharply with the 2000-m ridge case, in which there is zero interbasin exchange for $\theta \leq 0^\circ\text{C}$. Figures 9b–d show that the meridional isopycnal transports increase with the ridge height, and that the transport shifts to lighter densities. This is consistent with the strengthening of the model's overturning circulation and reduction of the isopycnal slope with ridge height, as discussed previously in section 3.

Figures 9e and 9f show that diapycnal transport is largely insensitive to ridge height in both magnitude and structure; with one exception being the diapycnal transport in the ACC box for the 2000-m ridge case, which is shifted to warmer isopycnals relative to the reference case and 250-m ridge case. From Fig. 6g, the northern subcell almost entirely subsumes the southern subcell in the 2000-m ridge case, and thus T_{ACC}^d and T_{gyre}^d are both computed within the northern subcell, which occupies a greater vertical extent in the domain, thus shifting the diapycnal transport to warmer isopycnals. The strengthening of the abyssal overturning with ridge height results in a slight variation in the transformation ratio, shown in Fig. 9g, for the 2000-m ridge case relative to the other cases where ridge height is the only varied parameter. The clearest difference between the cases with varying ridge height can be seen in the transport ratio, shown in Fig. 9h. Relative to the reference case, the 250-m ridge case has a significantly higher transport ratio, indicating a greater degree of zonal recirculation relative to meridional export of dense waters. Meanwhile, the 2000-m ridge case has a much smaller transport ratio, implying that higher ridges shield dense waters from recirculation most effectively. This aligns with our bulk analysis,

in which ridge height was also the strongest predictor of AABW transport ratio (Fig. 8).

We now discuss the dependence of the density-resolved transports on the diapycnal diffusivity. The structure of the interbasin exchange, shown in Fig. 9a, is largely unaffected by diffusivity. In contrast, Figs. 9b–d show that the temperatures at which the meridional isopycnal transport takes place increases substantially with the diffusivity. The diffusivity also strongly influences the density structure of the diapycnal transports, shown in Figs. 9e and 9f. For both the ACC box and the gyre box, increasing the diffusivity leads to a larger maximum diapycnal upwelling that occurs at lighter densities. This is consistent with advective–diffusive balance, which requires a greater diapycnal upwelling to balance the enhanced diffusivity at the seafloor.

Figures 9g and 9h show that transport ratio is relatively insensitive to the diffusivity, but the restructuring of the diapycnal transports as functions of density leads to substantial changes in the transformation ratio. Increasing the diffusivity qualitatively preserves the density dependence of R^d , but results in a transformation ratio of $R^d \approx 1$ (all inflowing water being transformed via diapycnal upwelling) at warmer temperatures. This sharpens the transition between $R^d \approx 1$ (at $\theta \approx -0.85^\circ\text{C}$ for $\kappa_{\text{max}} = 3 \times 10^{-4} \text{ m}^2 \text{ s}^{-1}$ and at $\theta \approx -0.4^\circ\text{C}$ for $\kappa_{\text{max}} = 3 \times 10^{-3} \text{ m}^2 \text{ s}^{-1}$) to $R^d \approx -1$, which consistently occurs around $\theta \approx 0^\circ\text{C}$. This sharpening of the R^d profile in density space corresponds to a reduction in the density stratification of the AABW layer as κ_{max} increases.

c. Transformation of AABW

In the previous subsection, we examined isopycnal and diapycnal transports as a function of density within a two-box budget defined across the model domain. This analysis revealed that different density classes of AABW behave differently, with denser bottom waters experiencing less interbasin exchange, more consistent northward export, and stronger upwelling relative to lighter overlying waters. We now examine the simulated transformation using a stricter definition of AABW as the northward-flowing component of the abyssal waters. We elucidate the transformation process by diagnosing changes in the mean potential temperature of these northward-flowing waters.

We first define the magnitude of the northward component of the AABW transport as

$$\psi_{\text{AABW}}^*(y) = \max_{\theta \leq 1^\circ\text{C}} \left(\oint \bar{V}_\theta^t dx \right). \quad (28)$$

We then define the transport-weighted potential temperature $\Theta_{\text{AABW}}(y)$ as

$$\Theta_{\text{AABW}}(y) = \frac{\int_{-\infty}^{\theta^*(y)} \frac{\partial \Psi}{\partial \theta} d\theta}{\int_{-\infty}^{\theta^*(y)} \frac{\partial \Psi}{\partial \theta} d\theta}. \quad (29)$$

Here θ^* is the top of the northward-flowing AABW layer, defined such that $\Psi[y, \theta^*(y)] = \psi_{\text{AABW}}^*(y)$. Figure 4b illustrates

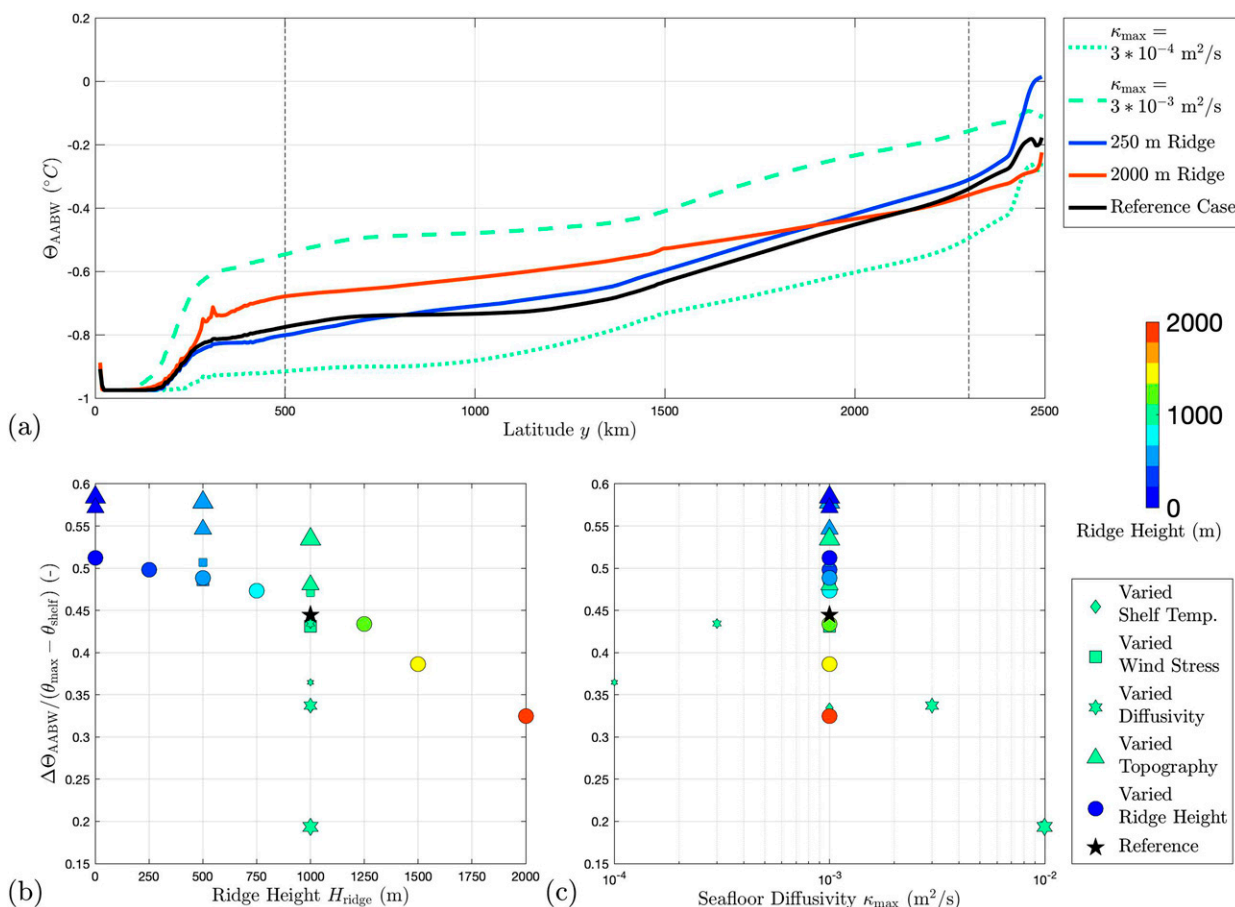


FIG. 10. Sensitivity of transport-weighted potential temperature to model parameters: (a) AABW transport-weighted potential temperature ($^{\circ}\text{C}$) as a function of latitude. Line style indicates ridge height and diffusivity perturbations. The dashed vertical lines indicate the shelf break ($y = 500$ km) and $y = 2300$ km, the latitudes between which we calculate our sensitivity diagnostic. Also shown is change in AABW transport-weighted potential temperature, normalized by the difference between the dynamically defined AABW potential temperature bound and imposed shelf temperature, plotted as a function of (b) ridge height and (c) seafloor diffusivity.

the latitudinal dependence of Θ_{AABW} in the reference simulation, and its relation to the isopycnal overturning streamfunction.

Figure 10a shows transport-weighted potential temperature as a function of latitude for a selection of experiments. In the reference case, Θ_{AABW} increases nearly monotonically with latitude, corresponding to a steady warming of the northward-flowing water. This is due to the continuous mixing of cold, dense waters with the warmer, light waters above along the pathway of the AABW. This mixing is structured by the presence of the two subcell abyssal overturning in the model, which controls the processes related to AABW density transformation. In the southern abyssal subcell, this mixing is associated with the upwelling of cold, dense water out of the northward-flowing AABW layer (see Fig. 4a). In the northern abyssal subcell, the mixing is associated with downwelling of the warm, light waters into the northward flowing layer, which leads to a more rapid change in Θ_{AABW} with latitude. The strength of these subcells and the latitude that separates them vary with both diffusivity magnitude (not shown) and ridge height (Fig. 6). This overturning structure

contributes to setting the overall transformation of AABW in the simulations.

Varying the ridge height has relatively little impact on the latitudinal profile of Θ_{AABW} , except in the latitude range of the ACC, where Θ_{AABW} is roughly 0.1°C warmer in the case of $H_{ridge} = 2000$ m. Varying the diffusivity has a much more pronounced effect on the magnitude of transport-weighted potential temperature: increasing κ_{max} to $3 \times 10^{-3} \text{ m}^2 \text{ s}^{-1}$ increases Θ_{AABW} by $0.15^{\circ}\text{--}0.2^{\circ}\text{C}$ throughout the model domain, whereas decreasing κ_{max} to $3 \times 10^{-4} \text{ m}^2 \text{ s}^{-1}$ decreases Θ_{AABW} by $0.15^{\circ}\text{--}0.2^{\circ}\text{C}$. These trends are consistent with the overall warming of the deep waters in the model domain as κ_{max} increases, due to increased mixing of the abyssal waters with overlying waters.

However, the transformation of AABW is measured by the change in Θ_{AABW} with latitude, rather than its average over the model domain. In Figs. 10b and 10c we therefore plot the sensitivity of the change in transport weighted potential temperature, calculated between $y = 500$ km and 2300 km (dashed vertical lines in Fig. 10a). This change in Θ_{AABW} is

normalized by the difference between imposed AABW formation temperature on the shelf (θ_{shelf}) and the dynamically defined AABW potential temperature bound (θ_{max}), that is, by the overall change in AABW temperature imposed by the northern and southern boundary restoring. The normalized change in transport-weighted potential temperature decreases with increasing ridge height and increases with increasing random topographic bump height. These sensitivities are consistent with the bathymetric influences on the AABW isopycnal slope shown in Figs. 6 and 7b. A possible explanation for this bathymetric influence on the transformation rate is that increasing the ridge height and removing the topographic bumps allows for more efficient northward flow in deep western boundary current conduits (see Fig. 2). This would decrease the time required for the average parcel of AABW to cross the domain, and thus reduce the cumulative mixing of the AABW with the overlying waters. Figure 10c shows that the normalized change in transport-weighted potential temperature depends nonmonotonically on κ_{max} . This suggests that stronger diapycnal diffusion may have competing influences on the AABW layer: while higher κ_{max} may be expected to increase the rate mixing of AABW with overlying waters and thus increase $\Delta\theta_{\text{AABW}}$, it may also decrease the potential temperature stratification of the abyssal ocean (without substantially changing the isopycnal slope, cf. Fig. 7b), and thus decrease $\Delta\theta_{\text{AABW}}$.

5. Discussion

a. Summary of key results

The motivation for this study was to examine the fundamental mechanisms governing AABW transport and transformation across the ACC. Formed in a handful of distinct sites on the Antarctic continental shelf, all AABW that reaches the northern ocean basins must first cross the ACC. Our central aim was to understand what parameters and dynamical processes set the connectivity of AABW sources between basins, the strength of AABW transport, and the degree of its transformation. In light of conflicting findings found in previous literature, we posed two extreme conceptions of the transfer of AABW across the ACC (Fig. 2): in one, the ACC functions as a blender, redistributing AABW zonally between different sectors of the ACC as it makes its way northward; in the other, the ACC serves as a conduit of AABW, by exporting it directly northward in deep western boundary currents supported by bathymetric features such as meridional ridges. We hypothesized that the height of bathymetry, relative to the thickness of the AABW layer, plays the determining role in this dynamical transition.

To address this hypothesis, we developed a highly idealized channel model, approximating a section of the ACC through Drake Passage (Fig. 3). In section 3, we examined the transport of AABW in this model from a bulk perspective, considering the behavior of all waters too cold to have been sourced from the northern boundary (approximately below 0°C for most model runs). The height of the meridional ridge emerged as the key parameter in setting the overturning circulation and

horizontal circulation within the AABW layer (Fig. 6). Though the pattern of overturning remains qualitatively similar for cases with varying ridge heights, we see an enhancement of overturning strength associated with higher ridges. The meridional export of AABW scales approximately linearly with ridge height (Fig. 7a), due to an increase in northward flow of AABW in the DWBC. Higher ridges are associated with a relaxation of abyssal AABW isopycnal slopes (Fig. 7b), and therefore a reduction in baroclinic instability. Both the increase in transport and reduction in isopycnal slope with ridge height are consistent with the increased efficiency of standing Rossby waves/meanders in transporting AABW northward (Fig. 7c).

The horizontal circulation within the AABW layer is also strongly influenced by the ridge height, with interbasin AABW exchange completely quashed by sufficiently high ridges (≥ 1250 m). By computing a transport ratio for AABW [(14)] and examining its sensitivity to model parameters, we found that the height of the meridional ridge is key, with higher ridges associated with low or zero values of the AABW transport ratio (Fig. 8). For low ridge heights with large AABW transport ratios, the AABW transport ratio varies linearly with the ACC transport. We developed a simplified equation for interbasin AABW exchange based upon the notion that AABW is passively advected by sea floor flow in the ACC, and therefore its magnitude is geometrically constrained by the elevation of bathymetry relative to AABW layer thickness. This simplified equation holds for cases with low meridional ridges and large interbasin exchanges, but underpredicts the exchange for cases with intermediate ridge heights (750 and 1000 m, see Fig. 8e). This suggests that more complicated dynamics govern the interbasin exchange of AABW where the height of meridional obstacles is comparable to AABW layer thickness.

In sections 4a and 4b we examined variations in meridional versus interbasin transport across different density classes within the AABW layer. Relative to lighter density classes, denser AABW is exported northward more consistently, exchanged over the ridge less readily, and transformed at a proportionally higher rate (Fig. 9). This analysis indicated that denser varieties of AABW have lower transport ratios, implying that they are more effectively shielded by the meridional ridge. In contrast, we found that the structure of the transformation ratio is strongly controlled by imposed vertical diffusivity. Consistent with advective–diffusive balance, this restructuring is primarily due to the reduction in the abyssal ocean stratification and enhancement of diapycnal transport as the diffusivity increases.

Our density-resolved analysis in sections 4a and 4b revealed that not all of the AABW within the bulk AABW layer is northward-flowing. This motivated us to explore to investigate the transformation of the northward-flowing component of AABW in section 4c. The overall transformation of the northward-flowing AABW decreases with increasing ridge height. This is consistent with the smaller abyssal isopycnal slopes at higher ridge heights (Fig. 7b), and suggests that the conduit established by the ridge allows AABW to cross the

ACC more rapidly, and thus subject to less mixing with overlying waters.

b. Limitations

By examining a simplified model, this work furthers our understanding of the fundamental mechanisms that give rise to AABW transport and transformation in the ACC. However, the highly idealized nature of the model also constrains the generalizability of these findings. The model geometry—including a rectangular domain and a rectangle in place of the southern tip of South America—is heavily simplified from the complex topography and bathymetry present in nature. Notably, lacking an Antarctic Peninsula, the model omits the subpolar gyres, which play a key role in ACC dynamics and overturning circulation (Wilson et al. 2022). We do not explore the effect of varying the width of the meridional ridge and continent, which has been shown to modify the ACC's barotropic transport and the structure of the subpolar gyres (Patmore et al. 2019). For the reference case, we also use a completely smooth sea floor, neglecting interactions of the AABW with rough topography such as lee wave generation and mixing (Mashayek et al. 2017; Yang et al. 2018). The cases with random seafloor topography partially address this, but do not resolve nor parameterize the response of internal wave generation and mixing to changes in the large-scale circulation. We do not vary the width of the topographic bumps, which could alter localized geostrophic transports. The model exhibits a two subcell abyssal overturning structure, and although this is consistent with the bottom-intensified mixing applied in these simulations, further observational evidence is required to determine if this structure exists in nature. The model also represents a simplified view of the thermodynamics of the ACC system: we use a one-dimensional, linear equation of state, which means the model neglects any dynamics arising from salinity variations in the ACC, and from nonlinearities in the equation of state (Groeskamp et al. 2016).

Our handling of boundary conditions also presents caveats to the study by producing some unrealistic structure in these simulations. By imposing a sponge layer in the northern edge of the domain, we do not resolve or parameterize any feedback processes from the northern basins. It is possible that this could impact dynamics on longer time scales, although recent research supports the dynamical independence of the overturning circulation of the Southern Ocean and that of the northern basins (Chang and Jansen 2021). By imposing a sponge layer in the southern edge of the domain, we neglect all processes concerning the formation of AABW and its pathways into the ACC. We endeavor to mitigate artificial effects by avoiding the continental shelf region ($y < 500$ km) in our analysis, and normalizing diagnostics (such as the change in transport-weighted potential temperature) by the difference between imposed shelf temperature and northern boundary temperature. The adjustment of the meridional overturning circulation to localized AABW source changes, and its associated time scales, poses an avenue for further investigation.

Our findings are further constrained by the spatial resolution of the model. The analysis presented in this study is based on the high-resolution runs, with a horizontal grid spacing of ~ 5 km, which resolves mesoscale eddies in the interior of the domain but neglects smaller-scale process that may affect AABW and ACC dynamics. The model grid is insufficient to resolve the scales of baroclinic eddy generation over the continental shelf. An important limitation is the model's inability to explicitly resolve AABW interactions with lee wave driven mixing (Yang et al. 2021; Broadbridge et al. 2016) and internal tides. This limitation has the potential to affect the degree of AABW transformation exhibited in the model, given the particularly important role of lee waves and their associated mixing in driving water-mass transformation in the Southern Ocean (Nikurashin and Ferrari 2013; de Lavergne et al. 2016).

The model is forced with time-invariant profiles of wind stress and surface buoyancy flux, and we compute all diagnostics from a 20-yr time-average of model output. Therefore, we neglect all seasonal and submonthly variability in ACC and AABW dynamics in our experimental design and analysis, which limits the applicability of our findings to nature. Measurements and modeling of AABW formation indicate significant seasonal and submonthly variations in formation and mixing (Budillon et al. 2011; Stewart 2021), which affects the thermodynamics of AABW as it is exported across the ASF and ACC. Additionally, on submonthly time scales the ACC transport fluctuates by $\pm 50\%$ of its mean value (Whitworth and Peterson 1985), and the northward AABW transport may exhibit subannual fluctuations that are comparable to the multiannual mean (Fukamachi et al. 2010; Stewart et al. 2021). The impact of this variability on interbasin versus meridional transport of AABW remains unclear.

c. Avenues for future research

Our findings provide insight into the dynamics of AABW in the ACC that are observed in the real ocean, as well as in high-resolution models that are designed to more closely mimic nature. Solodoch et al. (2022) deploy passive tracers in a global ocean/sea ice model to examine the pathways of AABW sourced from different locations around the Antarctic continental margins. This study identifies two major conduits responsible for the bulk of northward AABW export: Weddell Sea- and Prydz Bay-sourced AABW is blended together and transported into the Atlantic and Indian Oceans, whereas Ross Sea- and Adelie Land-sourced AABW is blended and transported into the Pacific Ocean. Our findings suggest that bathymetry plays a central role in this blending of AABW sources and its subsequent export in two primary northward conduits. This has broad implications for the global meridional overturning circulation, which is sensitive to changes in abyssal overturning in the Southern Ocean (Nadeau and Jansen 2020). Further study of the dynamical controls on the transport and transformation of AABW in the ACC, such as additional high-resolution tracer model runs, is required to translate our findings to the real ocean.

Of the parameters explored in our study, bathymetry exerts the strongest control over the dynamics of AABW transport

and transformation in the ACC. In particular, the height of the meridional ridge relative to AABW layer thickness controls the degree of interbasin exchange, which has implications for dynamics across a range of time scales. On time scales of decades to millennia, changes in the thickness of the AABW layer, for example due to changes in Antarctic shelf processes, could alter the dynamics of AABW across the ACC. Under the most likely climate change scenarios, AABW production is anticipated to decline or cease as a result of freshwater input from the melting of the Antarctic Ice Sheet (Lago and England 2019). The reduction of AABW formation would imply a thinner AABW layer, which our results link to a reduction in AABW interbasin exchange and density transformation. Observations have indicated that AABW has warmed and freshened over the last several decades (Purkey et al. 2019) with further changes in AABW density anticipated under climate change. Similarly, the AABW has been demonstrated to have been shallower, warmer, and fresher during the Last Glacial Maximum (Skinner et al. 2010; Huang et al. 2020). These changes in AABW layer thermodynamics, from both inferred past and projected future climates, has implications for the strength of the meridional overturning circulation in the Southern Ocean, as well as its ability to trap heat in the abyss.

Our results align with research demonstrating that shifts in the geometry of the Southern Ocean on geologic time scales have drastically altered the routing and mixing of AABW. The opening of Drake Passage, estimated to have taken place approximately 30 million years ago (Barker and Burrell 1977; Stickley et al. 2004), allowed for the formation of the ACC, which serves as the dominant feature of the Southern Ocean circulation and therefore a key mediator of global climate (Yang et al. 2014). This geologic shift has been associated with a weakening of the overturning circulation and a cooling of the Southern Hemisphere (Sijp and England 2005), as well as strong ocean/sea ice and albedo feedbacks that maintain cool ocean temperatures around the Antarctic continent conducive the formation of glaciers and ice sheets (England et al. 2017). The model results provide a dynamical interpretation of previous research that demonstrates a strengthening of meridional overturning circulation, and subsequently AABW northward export, as a result of enhanced meridional barriers to ACC flow.

In summary, our analysis of a process-oriented model of the ACC has demonstrated that the height of meridional barriers provides the strongest constraint on AABW transport and transformation in the ACC. Though highly idealized, the model accurately reproduces key features of ACC circulation, and provides insight into the fundamental mechanisms governing the dynamics of AABW. These results have implications for the meridional overturning circulation as well as global climate, as it existed in the past and is projected to exist in the future under anthropogenic climate change.

Acknowledgments. This material is based in part upon work supported by the National Science Foundation under Grant OPP-2023244, and by the National Aeronautics and

Space Administration ROSES Physical Oceanography program under Grant 80NSSC19K1192. This work used the Extreme Science and Engineering Discovery Environment (XSEDE; Towns et al. 2014), which is supported by National Science Foundation Grant ACI-1548562. Author A. F. Thompson acknowledges support from OPP-2023259. We thank the MITgcm team for their contribution to numerical modeling and for making their code available. Author Y. Si acknowledges support from the China Scholarship Council (201806010366).

Data availability statement. The source code of the Massachusetts Institute of Technology General Circulation Model (MITgcm) is available online (<http://mitgcm.org>), as are the model simulation data (<https://doi.org/10.15144/S43W2C>). The MATLAB scripts used to generate, run, and analyze the MITgcm simulations are also available online (<http://doi.org/10.5281/zenodo.6565001>).

REFERENCES

- Abernathy, R., and P. Cessi, 2014: Topographic enhancement of eddy efficiency in baroclinic equilibration. *J. Phys. Oceanogr.*, **44**, 2107–2126, <https://doi.org/10.1175/JPO-D-14-0014.1>.
- , J. Marshall, and D. Ferreira, 2011: The dependence of Southern Ocean meridional overturning on wind stress. *J. Phys. Oceanogr.*, **41**, 2261–2278, <https://doi.org/10.1175/JPO-D-11-023.1>.
- Abrahamsen, E. P., and Coauthors, 2019: Stabilization of dense Antarctic water supply to the Atlantic Ocean overturning circulation. *Nat. Climate Change*, **9**, 742–746, <https://doi.org/10.1038/s41558-019-0561-2>.
- Barker, P. F., and J. Burrell, 1977: The opening of Drake Passage. *Mar. Geol.*, **25**, 15–34, [https://doi.org/10.1016/0025-3227\(77\)90045-7](https://doi.org/10.1016/0025-3227(77)90045-7).
- Behrens, E., G. Rickard, O. Morgenstern, T. Martin, A. Osprey, and M. Joshi, 2016: Southern Ocean deep convection in global climate models: A driver for variability of subpolar gyres and Drake Passage transport on decadal timescales. *J. Geophys. Res. Oceans*, **121**, 3905–3925, <https://doi.org/10.1002/2015JC011286>.
- Bischoff, T., and A. F. Thompson, 2014: Configuration of a Southern Ocean storm track. *J. Phys. Oceanogr.*, **44**, 3072–3078, <https://doi.org/10.1175/JPO-D-14-0062.1>.
- Broadbridge, M. B., A. C. Naveira Garabato, and A. J. G. Nurser, 2016: Forcing of the overturning circulation across a circumpolar channel by internal wave breaking. *J. Geophys. Res. Oceans*, **121**, 5436–5451, <https://doi.org/10.1002/2015JC011597>.
- Budillon, G., P. Castagno, S. Aliani, G. Spezie, and L. Padman, 2011: Thermohaline variability and Antarctic Bottom Water formation at the Ross Sea shelf break. *Deep-Sea Res. I*, **58**, 1002–1018, <https://doi.org/10.1016/j.dsr.2011.07.002>.
- Cessi, P., 2019: The global overturning circulation. *Annu. Rev. Mar. Sci.*, **11**, 249–270, <https://doi.org/10.1146/annurev-marine-010318-095241>.
- Chang, C.-Y., and M. F. Jansen, 2021: Distinct controls on the strength of the abyssal overturning circulation: Channel versus basin dynamics. *J. Phys. Oceanogr.*, **51**, 2073–2086, <https://doi.org/10.1175/JPO-D-20-0316.1>.
- Cimoli, L., G. Gebbie, S. G. Purkey, and W. M. Smethie, 2023: Annually resolved propagation of CFCs and SF6 in the

- global ocean over eight decades. *J. Geophys. Res. Oceans*, **128**, e2022JC019337, <https://doi.org/10.1029/2022JC019337>.
- de Lavergne, C., J. B. Palter, E. D. Galbraith, R. Bernardello, and I. Marinov, 2014: Cessation of deep convection in the open Southern Ocean under anthropogenic climate change. *Nat. Climate Change*, **4**, 278–282, <https://doi.org/10.1038/nclimate2132>.
- , G. Madec, J. L. Sommer, A. J. G. Nurser, and A. C. Naveira Garabato, 2016: On the consumption of Antarctic Bottom Water in the abyssal ocean. *J. Phys. Oceanogr.*, **46**, 635–661, <https://doi.org/10.1175/JPO-D-14-0201.1>.
- Donohue, K. A., K. L. Tracey, D. R. Watts, M. P. Chidichimo, and T. K. Chereskin, 2016: Mean Antarctic Circumpolar Current transport measured in Drake Passage. *Geophys. Res. Lett.*, **43**, 11 760–11 767, <https://doi.org/10.1002/2016GL070319>.
- Döös, K., and D. J. Webb, 1994: The Deacon cell and the other meridional cells of the Southern Ocean. *J. Phys. Oceanogr.*, **24**, 429–442, [https://doi.org/10.1175/1520-0485\(1994\)024<0429:TDCATO>2.0.CO;2](https://doi.org/10.1175/1520-0485(1994)024<0429:TDCATO>2.0.CO;2).
- England, M. H., D. K. Hutchinson, A. Santoso, and W. P. Sijp, 2017: Ice–atmosphere feedbacks dominate the response of the climate system to Drake Passage closure. *J. Climate*, **30**, 5775–5790, <https://doi.org/10.1175/JCLI-D-15-0554.1>.
- Ferrari, R., M. F. Jansen, J. F. Adkins, A. Burke, A. L. Stewart, and A. F. Thompson, 2014: Antarctic sea ice control on ocean circulation in present and glacial climates. *Proc. Natl. Acad. Sci. USA*, **111**, 8753–8758, <https://doi.org/10.1073/pnas.1323922111>.
- , A. Mashayek, T. J. McDougall, M. Nikurashin, and J.-M. Campin, 2016: Turning ocean mixing upside down. *J. Phys. Oceanogr.*, **46**, 2239–2261, <https://doi.org/10.1175/JPO-D-15-0244.1>.
- Foppert, A., S. R. Rintoul, S. G. Purkey, N. Zilberman, T. Kobayashi, J.-B. Sallée, E. M. van Wijk, and L. O. Wallace, 2021: Deep Argo reveals bottom water properties and pathways in the Australian–Antarctic basin. *J. Geophys. Res. Oceans*, **126**, e2021JC017935, <https://doi.org/10.1029/2021JC017935>.
- Fukamachi, Y., S. R. Rintoul, J. A. Church, S. Aoki, S. Sokolov, M. A. Rosenberg, and M. Wakatsuchi, 2010: Strong export of Antarctic Bottom Water east of the Kerguelen Plateau. *Nat. Geosci.*, **3**, 327–331, <https://doi.org/10.1038/ngeo842>.
- Garcia, H., and Coauthors, 2018: *Dissolved Oxygen, Apparent Oxygen Utilization, and Dissolved Oxygen Saturation*. Vol. 3, *World Ocean Atlas 2018*, NOAA Atlas NESDIS 83, 38 pp.
- Gordon, A. L., E. Zambianchi, A. Orsi, M. Visbeck, C. F. Giulivi, T. Whitworth III, and G. Spezie, 2004: Energetic plumes over the western Ross Sea continental slope. *Geophys. Res. Lett.*, **31**, L21302, <https://doi.org/10.1029/2004GL020785>.
- Groeskamp, S., R. P. Abernathey, and A. Klocker, 2016: Water mass transformation by cabbeling and thermobaricity. *Geophys. Res. Lett.*, **43**, 10 835–10 845, <https://doi.org/10.1002/2016GL070860>.
- , S. M. Griffies, D. Iudicone, R. Marsh, A. J. G. Nurser, and J. D. Zika, 2019: The water mass transformation framework for ocean physics and biogeochemistry. *Annu. Rev. Mar. Sci.*, **11**, 271–305, <https://doi.org/10.1146/annurev-marine-010318-095421>.
- Hallberg, R., and A. Gnanadesikan, 2001: An exploration of the role of transient eddies in determining the transport of a zonally reentrant current. *J. Phys. Oceanogr.*, **31**, 3312–3330, [https://doi.org/10.1175/1520-0485\(2001\)031<3312:AEOTRO>2.0.CO;2](https://doi.org/10.1175/1520-0485(2001)031<3312:AEOTRO>2.0.CO;2).
- Hellmer, H. H., F. Kauker, R. Timmermann, J. Determann, and J. Rae, 2012: Twenty-first-century warming of a large Antarctic ice-shelf cavity by a redirected coastal current. *Nature*, **485**, 225–228, <https://doi.org/10.1038/nature11064>.
- , —, —, and T. Hattermann, 2017: The fate of the southern Weddell Sea continental shelf in a warming climate. *J. Climate*, **30**, 4337–4350, <https://doi.org/10.1175/JCLI-D-16-0420.1>.
- Hill, C., D. Ferreira, J.-M. Campin, J. Marshall, R. Abernathey, and N. Barrier, 2012: Controlling spurious diapycnal mixing in eddy-resolving height-coordinate ocean models — Insights from virtual deliberate tracer release experiments. *Ocean Modell.*, **45–46**, 14–26, <https://doi.org/10.1016/j.ocemod.2011.12.001>.
- Howard, E., A. M. Hogg, S. Waterman, and D. P. Marshall, 2015: The injection of zonal momentum by buoyancy forcing in a Southern Ocean model. *J. Phys. Oceanogr.*, **45**, 259–271, <https://doi.org/10.1175/JPO-D-14-0098.1>.
- Huang, H., M. Gutjahr, A. Eisenhauer, and G. Kuhn, 2020: No detectable Weddell Sea Antarctic Bottom Water export during the Last and penultimate glacial maximum. *Nat. Commun.*, **11**, 424, <https://doi.org/10.1038/s41467-020-14302-3>.
- Ito, T., and J. Marshall, 2008: Control of lower-limb overturning circulation in the Southern Ocean by diapycnal mixing and mesoscale eddy transfer. *J. Phys. Oceanogr.*, **38**, 2832–2845, <https://doi.org/10.1175/2008JPO3878.1>.
- Jackett, D. R., and T. J. McDougall, 1997: A neutral density variable for the world's oceans. *J. Phys. Oceanogr.*, **27**, 237–263, [https://doi.org/10.1175/1520-0485\(1997\)027<0237:ANDVFT>2.0.CO;2](https://doi.org/10.1175/1520-0485(1997)027<0237:ANDVFT>2.0.CO;2).
- Johnson, G. C., 2008: Quantifying Antarctic Bottom Water and North Atlantic deep water volumes. *J. Geophys. Res.*, **113**, C05027, <https://doi.org/10.1029/2007JC004477>.
- Jouanno, J., and X. Capet, 2020: Connecting flow–topography interactions, vorticity balance, baroclinic instability and transport in the Southern Ocean: The case of an idealized storm track. *Ocean Sci.*, **16**, 1207–1223, <https://doi.org/10.5194/os-16-1207-2020>.
- Kiss, A. E., and Coauthors, 2020: ACCESS-OM2: A global ocean–sea ice model at three resolutions. *Geosci. Model Dev.*, **13**, 401–442, <https://doi.org/10.5194/gmd-13-401-2020>.
- Kusahara, K., G. D. Williams, T. Tamura, R. Massom, and H. Hasumi, 2017: Dense shelf water spreading from Antarctic coastal polynyas to the deep Southern Ocean: A regional circumpolar model study. *J. Geophys. Res. Oceans*, **122**, 6238–6253, <https://doi.org/10.1002/2017JC012911>.
- Lago, V., and M. H. England, 2019: Projected slowdown of Antarctic Bottom Water formation in response to amplified meltwater contributions. *J. Climate*, **32**, 6319–6335, <https://doi.org/10.1175/JCLI-D-18-0622.1>.
- Large, W. G., and S. G. Yeager, 2009: The global climatology of an interannually varying air–sea flux data set. *Climate Dyn.*, **33**, 341–364, <https://doi.org/10.1007/s00382-008-0441-3>.
- , J. C. McWilliams, and S. C. Doney, 1994: Oceanic vertical mixing: A review and a model with a nonlocal boundary layer parameterization. *Rev. Geophys.*, **32**, 363–403, <https://doi.org/10.1029/94RG01872>.
- Locarnini, R., and Coauthors, 2019: *Density*. Vol. 5, *World Ocean Atlas 2018*, NOAA Atlas NESDIS 85, 51 pp.
- Lumpkin, R., and K. Speer, 2007: Global Ocean meridional overturning. *J. Phys. Oceanogr.*, **37**, 2550–2562, <https://doi.org/10.1175/JPO3130.1>.
- Lynch-Stieglitz, J., T. Ito, and E. Michel, 2016: Antarctic density stratification and the strength of the circumpolar current during the Last Glacial Maximum. *Paleoceanography*, **31**, 539–552, <https://doi.org/10.1002/2015PA002915>.

- Marshall, D. P., M. H. P. Ambaum, J. R. Maddison, D. R. Munday, and L. Novak, 2017: Eddy saturation and frictional control of the Antarctic Circumpolar Current. *Geophys. Res. Lett.*, **44**, 286–292, <https://doi.org/10.1002/2016GL071702>.
- Marshall, J., and T. Radko, 2003: Residual-mean solutions for the Antarctic Circumpolar Current and its associated overturning circulation. *J. Phys. Oceanogr.*, **33**, 2341–2354, [https://doi.org/10.1175/1520-0485\(2003\)033<2341:RSFTAC>2.0.CO;2](https://doi.org/10.1175/1520-0485(2003)033<2341:RSFTAC>2.0.CO;2).
- , and K. Speer, 2012: Closure of the meridional overturning circulation through Southern Ocean upwelling. *Nat. Geosci.*, **5**, 171–180, <https://doi.org/10.1038/ngeo1391>.
- , A. Adcroft, C. Hill, L. Perelman, and C. Heisey, 1997a: A finite-volume, incompressible Navier Stokes model for studies of the ocean on parallel computers. *J. Geophys. Res.*, **102**, 5753–5766, <https://doi.org/10.1029/96JC02775>.
- , C. Hill, L. Perelman, and A. Adcroft, 1997b: Hydrostatic, quasi-hydrostatic, and nonhydrostatic ocean modeling. *J. Geophys. Res.*, **102**, 5733–5752, <https://doi.org/10.1029/96JC02776>.
- Mashayek, A., R. Ferrari, M. Nikurashin, and W. R. Peltier, 2015: Influence of enhanced abyssal diapycnal mixing on stratification and the ocean overturning circulation. *J. Phys. Oceanogr.*, **45**, 2580–2597, <https://doi.org/10.1175/JPO-D-15-0039.1>.
- , —, S. Merrifield, J. R. Ledwell, L. St Laurent, and A. N. Garabato, 2017: Topographic enhancement of vertical turbulent mixing in the Southern Ocean. *Nat. Commun.*, **8**, 14197, <https://doi.org/10.1038/ncomms14197>.
- Meredith, M. P., and A. M. Hogg, 2006: Circumpolar response of Southern Ocean eddy activity to a change in the Southern Annular Mode. *Geophys. Res. Lett.*, **33**, L16608, <https://doi.org/10.1029/2006GL026499>.
- Morrison, A. K., and A. M. Hogg, 2013: On the relationship between Southern Ocean overturning and ACC transport. *J. Phys. Oceanogr.*, **43**, 140–148, <https://doi.org/10.1175/JPO-D-12-057.1>.
- , —, and M. L. Ward, 2011: Sensitivity of the Southern Ocean overturning circulation to surface buoyancy forcing. *Geophys. Res. Lett.*, **38**, L14602, <https://doi.org/10.1029/2011GL048031>.
- , M. H. England, and A. M. Hogg, 2015: Response of Southern Ocean convection and abyssal overturning to surface buoyancy perturbations. *J. Climate*, **28**, 4263–4278, <https://doi.org/10.1175/JCLI-D-14-00110.1>.
- Munday, D. R., H. L. Johnson, and D. P. Marshall, 2013: Eddy saturation of equilibrated circumpolar currents. *J. Phys. Oceanogr.*, **43**, 507–532, <https://doi.org/10.1175/JPO-D-12-095.1>.
- Munk, W. H., 1966: Abyssal recipes. *Deep-Sea Res. Oceanogr. Abstr.*, **13**, 707–730, [https://doi.org/10.1016/0011-7471\(66\)90602-4](https://doi.org/10.1016/0011-7471(66)90602-4).
- Nadeau, L.-P., and M. F. Jansen, 2020: Overturning circulation pathways in a two-basin ocean model. *J. Phys. Oceanogr.*, **50**, 2105–2122, <https://doi.org/10.1175/JPO-D-20-0034.1>.
- Newsom, E. R., C. M. Bitz, F. O. Bryan, R. Abernathey, and P. R. Gent, 2016: Southern Ocean deep circulation and heat uptake in a high-resolution climate model. *J. Climate*, **29**, 2597–2619, <https://doi.org/10.1175/JCLI-D-15-0513.1>.
- Nicholls, K. W., S. Østerhus, K. Makinson, T. Gammelsrød, and E. Fahrbach, 2009: Ice-ocean processes over the continental shelf of the southern Weddell Sea, Antarctica: A review. *Rev. Geophys.*, **47**, RG3003, <https://doi.org/10.1029/2007RG000250>.
- Nikurashin, M., and G. Vallis, 2011: A theory of deep stratification and overturning circulation in the ocean. *J. Phys. Oceanogr.*, **41**, 485–502, <https://doi.org/10.1175/2010JPO4529.1>.
- , and G. K. Vallis, 2012: A theory of the interhemispheric meridional overturning circulation and associated stratification. *J. Phys. Oceanogr.*, **42**, 1652–1667, <https://doi.org/10.1175/JPO-D-11-0189.1>.
- , and R. Ferrari, 2013: Overturning circulation driven by breaking internal waves in the deep ocean. *Geophys. Res. Lett.*, **40**, 3133–3137, <https://doi.org/10.1002/grl.50542>.
- Nurser, A. J. G., and M. M. Lee, 2004: Isopycnal averaging at constant height. Part I: The formulation and a case study. *J. Phys. Oceanogr.*, **34**, 2721–2739, <https://doi.org/10.1175/JPO2649.1>.
- Ohshima, K. I., and Coauthors, 2013: Antarctic Bottom Water production by intense sea-ice formation in the Cape Darnley polynya. *Nat. Geosci.*, **6**, 235–240, <https://doi.org/10.1038/ngeo1738>.
- Orsi, A. H., W. D. Nowlin, and T. Whitworth, 1993: On the circulation and stratification of the Weddell Gyre. *Deep-Sea Res. I*, **40**, 169–203, [https://doi.org/10.1016/0967-0637\(93\)90060-G](https://doi.org/10.1016/0967-0637(93)90060-G).
- , T. Whitworth III, and W. D. Nowlin Jr., 1995: On the meridional extent and fronts of the Antarctic Circumpolar Current. *Deep-Sea Res. I*, **42**, 641–673, [https://doi.org/10.1016/0967-0637\(95\)00021-W](https://doi.org/10.1016/0967-0637(95)00021-W).
- , G. C. Johnson, and J. L. Bullister, 1999: Circulation, mixing, and production of Antarctic Bottom Water. *Prog. Oceanogr.*, **43**, 55–109, [https://doi.org/10.1016/S0079-6611\(99\)00004-X](https://doi.org/10.1016/S0079-6611(99)00004-X).
- Patmore, R. D., P. R. Holland, D. R. Munday, A. C. N. Garabato, D. P. Stevens, and M. P. Meredith, 2019: Topographic control of Southern Ocean gyres and the Antarctic Circumpolar Current: A barotropic perspective. *J. Phys. Oceanogr.*, **49**, 3221–3244, <https://doi.org/10.1175/JPO-D-19-0083.1>.
- Pedlosky, J., 1990: The dynamics of the oceanic subtropical gyres. *Science*, **248**, 316–322, <https://doi.org/10.1126/science.248.4953.316>.
- Prather, M. J., 1986: Numerical advection by conservation of second-order moments. *J. Geophys. Res.*, **91**, 6671–6681, <https://doi.org/10.1029/JD091iD06p06671>.
- Purkey, S. G., and G. C. Johnson, 2013: Antarctic Bottom Water warming and freshening: Contributions to sea level rise, ocean freshwater budgets, and global heat gain. *J. Climate*, **26**, 6105–6122, <https://doi.org/10.1175/JCLI-D-12-00834.1>.
- , —, L. D. Talley, B. M. Sloyan, S. E. Wijffels, W. Smethie, S. Mecking, and K. Katsumata, 2019: Unabated bottom water warming and freshening in the South Pacific Ocean. *J. Geophys. Res. Oceans*, **124**, 1778–1794, <https://doi.org/10.1029/2018JC014775>.
- Rintoul, S. R., 1985: On the origin and influence of Adélie Land Bottom Water. *Ocean, Ice, and Atmosphere: Interactions at the Antarctic Continental Margin*, S. S. Jacobs and R. F. Weiss, Eds., Antarctic Research Series, Vol. 75, Amer. Geophys. Union, 151–171.
- Sijp, W. P., and M. H. England, 2005: Role of the Drake Passage in controlling the stability of the ocean's thermohaline circulation. *J. Climate*, **18**, 1957–1966, <https://doi.org/10.1175/JCLI3376.1>.
- Skinner, L., S. Fallon, C. Waelbroeck, E. Michel, and S. Barker, 2010: Ventilation of the deep Southern Ocean and deglacial CO₂ rise. *Science*, **328**, 1147–1151, <https://doi.org/10.1126/science.1183627>.
- Snow, K., S. R. Rintoul, B. M. Sloyan, and A. M. Hogg, 2018: Change in dense shelf water and Adélie Land bottom water precipitated by iceberg calving. *Geophys. Res. Lett.*, **45**, 2380–2387, <https://doi.org/10.1002/2017GL076195>.
- Solodoch, A., A. L. Stewart, A. M. Hogg, A. K. Morrison, A. E. Kiss, A. F. Thompson, S. G. Purkey, and L. Cimoli, 2022: How does Antarctic Bottom Water cross the Southern

- Ocean? *Geophys. Res. Lett.*, **49**, e2021GL097211, <https://doi.org/10.1029/2021GL097211>.
- Stewart, A. L., 2021: Mesoscale, tidal and seasonal/interannual drivers of the Weddell Sea overturning circulation. *J. Phys. Oceanogr.*, **51**, 3695–3722, <https://doi.org/10.1175/JPO-D-20-0320.1>.
- , and A. F. Thompson, 2012: Sensitivity of the ocean's deep overturning circulation to easterly Antarctic winds. *Geophys. Res. Lett.*, **39**, L18604, <https://doi.org/10.1029/2012GL053099>.
- , and —, 2013: Connecting Antarctic cross-slope exchange with Southern Ocean overturning. *J. Phys. Oceanogr.*, **43**, 1453–1471, <https://doi.org/10.1175/JPO-D-12-0205.1>.
- , and A. M. Hogg, 2017: Reshaping the Antarctic Circumpolar Current via Antarctic Bottom Water Export. *J. Phys. Oceanogr.*, **47**, 2577–2601, <https://doi.org/10.1175/JPO-D-17-0007.1>.
- , R. Ferrari, and A. F. Thompson, 2014: On the importance of surface forcing in conceptual models of the deep ocean. *J. Phys. Oceanogr.*, **44**, 891–899, <https://doi.org/10.1175/JPO-D-13-0206.1>.
- , X. Chi, A. Solodoch, and A. M. Hogg, 2021: High-frequency fluctuations in Antarctic Bottom Water transport driven by Southern Ocean Winds. *Geophys. Res. Lett.*, **48**, e2021GL094569, <https://doi.org/10.1029/2021GL094569>.
- Stickley, C. E., and Coauthors, 2004: Timing and nature of the deepening of the Tasmanian Gateway. *Paleoceanography*, **19**, PA4027, <https://doi.org/10.1029/2004PA001022>.
- Sun, S., I. Eisenman, L. Zanna, and A. L. Stewart, 2020: Surface constraints on the depth of the Atlantic meridional overturning circulation: Southern Ocean versus North Atlantic. *J. Climate*, **33**, 3125–3149, <https://doi.org/10.1175/JCLI-D-19-0546.1>.
- Talley, L. D., 2013: Closure of the global overturning circulation through the Indian, Pacific, and Southern Oceans: Schematics and transports. *Oceanography*, **26**, 80–97, <https://doi.org/10.5670/oceanog.2013.07>.
- , G. L. Pickard, and W. J. Emery, 2011: *Descriptive Physical Oceanography: An Introduction*. Academic Press, 555 pp.
- Thompson, A. F., and A. C. Naveira Garabato, 2014: Equilibration of the Antarctic Circumpolar Current by standing meanders. *J. Phys. Oceanogr.*, **44**, 1811–1828, <https://doi.org/10.1175/JPO-D-13-0163.1>.
- , A. L. Stewart, and T. Bischoff, 2016: A multi-basin residual-mean model for the global overturning circulation. *J. Phys. Oceanogr.*, **46**, 2583–2604, <https://doi.org/10.1175/JPO-D-15-0204.1>.
- , —, P. Spence, and K. J. Heywood, 2018: The Antarctic slope front in a changing climate. *Rev. Geophys.*, **56**, 741–770, <https://doi.org/10.1029/2018RG000624>.
- Towns, J., and Coauthors, 2014: XSEDE: Accelerating scientific discovery. *Comput. Sci. Eng.*, **16**, 62–74, <https://doi.org/10.1109/MCSE.2014.80>.
- Vallis, G. K., 2006: *Atmospheric and Oceanic Fluid Dynamics: Fundamentals and Large-Scale Circulation*. Cambridge University Press, 745 pp.
- van Sebillé, E., P. Spence, M. R. Mazloff, M. H. England, S. R. Rintoul, and O. A. Saenko, 2013: Abyssal connections of Antarctic Bottom Water in a Southern Ocean state estimate. *Geophys. Res. Lett.*, **40**, 2177–2182, <https://doi.org/10.1002/grl.50483>.
- Viebahn, J., and C. Eden, 2012: Standing eddies in the meridional overturning circulation. *J. Phys. Oceanogr.*, **42**, 1486–1508, <https://doi.org/10.1175/JPO-D-11-087.1>.
- Whitworth, T., III, and R. G. Peterson, 1985: Volume transport of the Antarctic Circumpolar Current from bottom pressure measurements. *J. Phys. Oceanogr.*, **15**, 810–816, [https://doi.org/10.1175/1520-0485\(1985\)015<0810:VTOTAC>2.0.CO;2](https://doi.org/10.1175/1520-0485(1985)015<0810:VTOTAC>2.0.CO;2).
- Williams, G. D., S. Aoki, S. S. Jacobs, S. R. Rintoul, T. Tamura, and N. L. Bindoff, 2010: Antarctic bottom water from the Adélie and George V Land coast, East Antarctica (140–149°E). *J. Geophys. Res.*, **115**, C04027, <https://doi.org/10.1029/2009JC005812>.
- Wilson, E. A., A. F. Thompson, A. L. Stewart, and S. Sun, 2022: Bathymetric control of subpolar gyres and the overturning circulation in the Southern Ocean. *J. Phys. Oceanogr.*, **52**, 205–223, <https://doi.org/10.1175/JPO-D-21-0136.1>.
- Wolfe, C. L., 2014: Approximations to the ocean's residual circulation in arbitrary tracer coordinates. *Ocean Modell.*, **75**, 20–35, <https://doi.org/10.1016/j.ocemod.2013.12.004>.
- Wunsch, C., and R. Ferrari, 2004: Vertical mixing, energy, and the general circulation of the oceans. *Annu. Rev. Fluid Mech.*, **36**, 281–314, <https://doi.org/10.1146/annurev.fluid.36.050802.122121>.
- Yang, L., M. Nikurashin, A. M. Hogg, and B. M. Sloyan, 2018: Energy loss from transient eddies due to lee wave generation in the Southern Ocean. *J. Phys. Oceanogr.*, **48**, 2867–2885, <https://doi.org/10.1175/JPO-D-18-0077.1>.
- , —, —, and —, 2021: The impact of lee waves on the Southern Ocean circulation. *J. Phys. Oceanogr.*, **51**, 2933–2950, <https://doi.org/10.1175/JPO-D-20-0263.1>.
- Yang, S., E. Galbraith, and J. Palter, 2014: Coupled climate impacts of the Drake Passage and the Panama Seaway. *Climate Dyn.*, **43**, 37–52, <https://doi.org/10.1007/s00382-013-1809-6>.
- Zhang, X., and M. Nikurashin, 2020: Small-scale topographic form stress and local dynamics of the Southern Ocean. *J. Geophys. Res. Oceans*, **125**, e2019JC015420, <https://doi.org/10.1029/2019JC015420>.